

AD-A070 590

STD RESEARCH CORP ARCADIA CALIF

F/6 20/9

MAGNETOHYDRODYNAMIC PHENOMENA IN PULSED MHD FLOWS. (U)

JAN 78 S T DEMETRIADES, D M MARKHAM

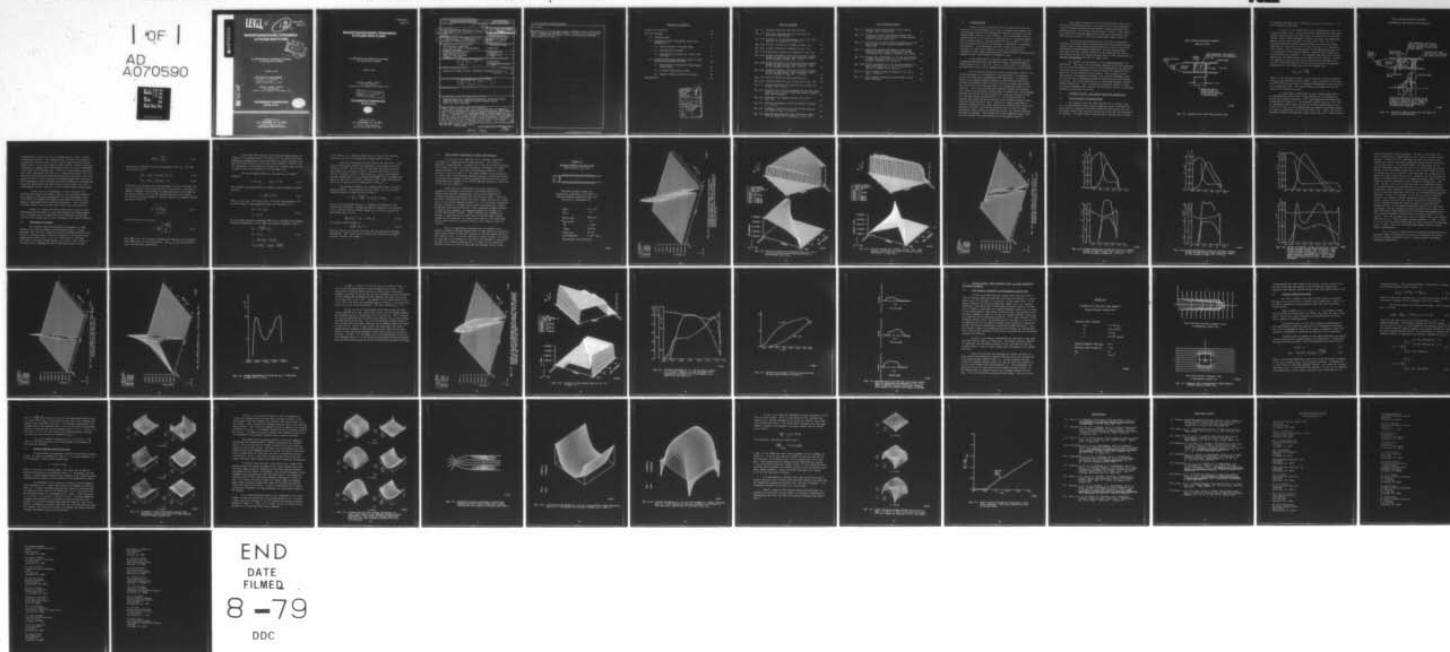
N00014-77-C-0574

UNCLASSIFIED

STD-UP-002-77-1

NL

| QF |
AD
A070590



ADA070590

LEVEL II

12

STD-UP-002-77-1

STDR-79-2

MAGNETOGASDYNAMIC PHENOMENA IN PULSED MHD FLOWS



S.T. DEMETRIADES, D.M. MARKHAM, C.D. MAXWELL
D.A. OLIVER, AND T.F. SWEAN

JANUARY 1979

This document has been approved
for public release and sale; its
distribution is unlimited.

INTERIM SUMMARY REPORT
FOR THE PERIOD
1 AUGUST 1977 THROUGH 31 OCTOBER 1978

DDC FILE COPY

STD RESEARCH CORPORATION

ARCADIA, CA 91006



Prepared for the
U.S. DEPARTMENT OF THE NAVY
Office of Naval Research
Under Contract N00014-77-C-0574

MAGNETOGASDYNAMIC PHENOMENA IN PULSED MHD FLOWS

**S.T. DEMETRIADES, D.M. MARKHAM, C.D. MAXWELL
D.A. OLIVER, AND T.F. SWEAN**

JANUARY 1979

**INTERIM SUMMARY REPORT
FOR THE PERIOD
1 AUGUST 1977 THROUGH 31 OCTOBER 1978**

*This document has been approved
for public release and sale; its
distribution is unlimited.*

**STD RESEARCH CORPORATION
ARCADIA, CA 91006**



**Prepared for the
U.S. DEPARTMENT OF THE NAVY
Office of Naval Research
Under Contract N00014-77-C-0574**

REPORT DOCUMENTATION PAGE		READ INSTRUCTIONS BEFORE COMPLETING FORM
1. REPORT NUMBER	2. GOVT ACCESSION NO.	3. RECIPIENT'S CATALOG NUMBER
4. TITLE (and Subtitle)		5. TYPE OF REPORT & PERIOD COVERED
6 Magnetogasdynamic Phenomena in Pulsed MHD Flows		Interim Summary Report. 1 Aug 77 through 31 Oct 78
7. AUTHOR(s)		8. CONTRACT OR GRANT NUMBER(s)
10 S.T. Demetriades, D.M. Markham, C.D. Maxwell, D.A. Oliver, T.F. Swean		15 STD-UP-002-77-1 N00014-77-C-0574
9. PERFORMING ORGANIZATION NAME AND ADDRESS		10. PROGRAM ELEMENT, PROJECT, TASK AREA & WORK UNIT NUMBERS
STD Research Corporation P.O. Box "C" (150 E. Foothill Blvd.) Arcadia, CA 91006		NR099-415
11. CONTROLLING OFFICE NAME AND ADDRESS		12. REPORT DATE
Department of the Navy Office of Naval Research Arlington, VA 22217		November 1978
14. MONITORING AGENCY NAME & ADDRESS (if different from Controlling Office)		13. NUMBER OF PAGES
11 Jan 78		55
16. DISTRIBUTION STATEMENT (of this Report)		15. SECURITY CLASS. (of this report)
Approved for public release; distribution unlimited		Unclassified
17. DISTRIBUTION STATEMENT (of the abstract entered in Block 20, if different from Report)		15a. DECLASSIFICATION/DOWNGRADING SCHEDULE
14 STD-UP-002-77-1, STDR-79-2		
18. SUPPLEMENTARY NOTES		
19. KEY WORDS (Continue on reverse side if necessary and identify by block number)		
Magnetogasdynamics, Magnetohydrodynamics, Pulsed MHD Flows, Explosive MHD, High Magnetic Reynolds Number Flows, Shock Tube MHD Generator		
20. ABSTRACT (Continue on reverse side if necessary and identify by block number)		
This report examines some of the detailed structure of magnetogasdynamic flows encountered in pulsed magnetohydrodynamic (MHD) generators. Two illustrations of magnetogasdynamic nonuniformities are considered. The first is for conventional explosive-driven MHD generators. Here we reveal the detailed structure of the deceleration of the conducting slug formed by the compression of plasma between the explosive-driven shock wave and its following contact surface. The second		

400 046

Lm

20. (cont'd)


Illustration is for steady high Magnetic Reynolds Number channel flows. Here we exhibit the nonuniform manner in which the external magnetic field is diffused into the plasma and the corresponding nonuniform deceleration of the flow. 

TABLE OF CONTENTS

TABLE OF CONTENTS	ii
LIST OF FIGURES	iii
1.0 INTRODUCTION	1
2.0 UNSTEADY FLOW: THE SHOCK TUBE MHD GENERATOR	2
2.1 Characterization of Nonuniformities	2
2.2 Mathematical Description	6
2.3 Flow Structure Prediction in a Shock Tube Generator	10
3.0 STEADY FLOW: MHD CHANNEL FLOW AT HIGH MAGNETIC REYNOLDS NUMBER	29
3.1 Flow Structure Prediction in Hydromagnetic Channel Flow	29
3.2 A Reduced Mathematical Model	32
3.3 Magnetic Diffusion and Flow Interaction	34
REFERENCES	44

Accession For	
NTIS GRA&I	<input checked="checked" type="checkbox"/>
DDC TAB	<input type="checkbox"/>
Unannounced	<input type="checkbox"/>
Justification	
By _____	
Distribution/ _____	
Availability Codes	
Dist.	Avail and/or special
A	

LIST OF FIGURES

Fig. 2-1. Idealized shock tube MHD generator flow	3
Fig. 2-2. Shock-tube MHD generator flow with fluid and electrical nonuniformities	5
Fig. 2-3a. Evolution of current distribution in shock tube MHD generator for conditions of Table 2-1.	12
Fig. 2-3b. Pressure evolution for conditions of Fig. 2-3a.	13
Fig. 2-3c. Velocity evolution for conditions of Fig. 2-3a.	14
Fig. 2-3d. Temperature evolution for conditions of Fig. 2-3a.	15
Fig. 2-4a. Detailed distribution of fluid and electrical variables through the high velocity, high temperature region for the evolution of Figs. 2-3. $t = \mu s$	16
Fig. 2-4b. Detailed distribution of fluid and electrical variables through the high velocity, high temperature region for the evolution in Figs. 2-3. $t = 70 \mu s$	17
Fig. 2-4c. Detailed distribution of fluid and electrical variables through the high velocity, high temperature region for the evolution in Figs. 2-3. $t = 140 \mu s$	18
Fig. 2-5a. Current evolution for high interaction case.	20
Fig. 2-5b. Velocity evolution for $B_0 = 3$ tesla case in Fig. 2-5a	21
Fig. 2-6. Detailed distribution of current for $B_0 = 3$ tesla case in Fig. 2-5a, $t = 90 \mu s$	22
Fig. 2-7a. Evolution of the current distribution for the case shown shown in Figs. 2-3 and 2-4 but with induced magnetic field effects included.	24
Fig. 2-7b. Evolution of the magnetic field for the case of Fig. 2-7a	25
Fig. 2-8. Detailed distribution of fluid and electrical variables at $t = 140 \mu s$	26
Fig. 2-9. Evolution of the total current and energy during the run shown in Figs. 2-3 and 2-4	27
Fig. 2-10. Experimentally observed total current pulse shapes from the experiments of Bangerter, et al., [5]	28

List of Figures (cont'd)

Fig. 3-1.	Magnetic field nonuniformities in high magnetic Reynolds number channel flow	31
Fig. 3-2.	Transverse current and external magnetic field distribution at three axial stations in high magnetic Reynolds number channel flow	35
Fig. 3-3.	Lorentz force and axial velocity distributions at three axial stations in high magnetic Reynolds number channel flow	37
Fig. 3-4.	Conjectured velocity streamlines in stalled high Magnetic Reynolds number channel flow showing recirculation cells trapped in boundary layer region	38
Fig. 3-5a.	Lorentz force distribution at $x = 21$ cm corresponding to higher interaction case ($\sigma = 2 \times 10^5$ mho/m) but otherwise conditions as in Table 3-1	39
Fig. 3-5b.	Velocity distribution at $x = 21$ cm corresponding to a higher interaction case ($\sigma = 2 \times 10^5$ mho/m) but otherwise conditions as in Table 3-1	40
Fig. 3-6.	Power extraction density evolution for the case in Figs. 3-2 and 3-3	42
Fig. 3-7.	Ratio of power extraction per unit length to ideal power extraction.	43

1.0 INTRODUCTION

Advances in the performance levels of devices based upon the interaction of electromagnetic forces with a conducting fluid depend in no small measure upon the understanding and control of electrical and fluid nonuniformities present in such machines. Such nonuniformities may be spatially induced by the presence of boundary walls or externally imposed fields (boundary layers, separation/interaction zones, wakes); or they may be temporally induced by the presence of instabilities or gasdynamic discontinuities. Such instabilities can lead to large scale coherent structures or small scale structures we may more properly term "turbulence"—either electromagnetic and/or fluid mechanical (electrothermal, magneto-acoustic, hydromagnetic instabilities; arcs).

In the present work we examine, some of the detailed structure of magnetogasdynamic flows encountered in pulsed magnetohydrodynamic (MHD) generators [1], [2], [3]. We do so with an eye to revealing the nonuniformities which may be significant in the operation of actual devices.

STD Research personnel have devoted considerable research to the detailed prediction of the phenomena in and performance of combustion-driven and closed-cycle nonequilibrium MHD generators. An important aspect of the detailed predictive approach is that important effects were predicted and exhibited before they were observed in actual experiments; hence they serve as an important guide to the fundamental design of such machines. These effects include inter-electrode shorting and breakdown [4], Lorentz force generated velocity profile overshoots (and correspondingly enhanced wall friction and heat transfer) [5], transverse electrode arcing [6], and MHD driven secondary flows [7]. In the present work we describe some initial efforts to bring this same predictive approach to bear upon pulsed MHD generator flows. Because of a prime requirement to minimize computation costs, these studies were conducted with reduced and simplified versions of the full STD Research codes in which full multi-dimensional effects, kinetic and diffusional effects, and detailed turbulence modeling are included. Nevertheless they reveal significant effects which the more detailed code implementations can subsequently elaborate.

Dense plasmas which serve as the working fluid for a class of these devices pose important questions as to the precise value of the equilibrium electrical conductivity which exists at attainable explosion generated states (plasma pressure ~ 10 - 100 k bar, plasma energy ~ 5 - 10 eV). Various theoretical estimates show that the highly compressed plasma conductivities may differ by nearly a factor of 2 from the classical Spitzer H \ddot{a} rm values [5].

As a contrast to these dense plasma corrections in equilibrium properties we will show that in the dynamical or flow state important internal structure exists in both unsteady shocked MHD flows as well as steady state high Magnetic Reynolds Number channel flow. The flow nonuniformities associated with these structures induced by the dynamical interaction of the working fluid with the external magnetic field can alter performance by an order of magnitude from that for uniform flow.

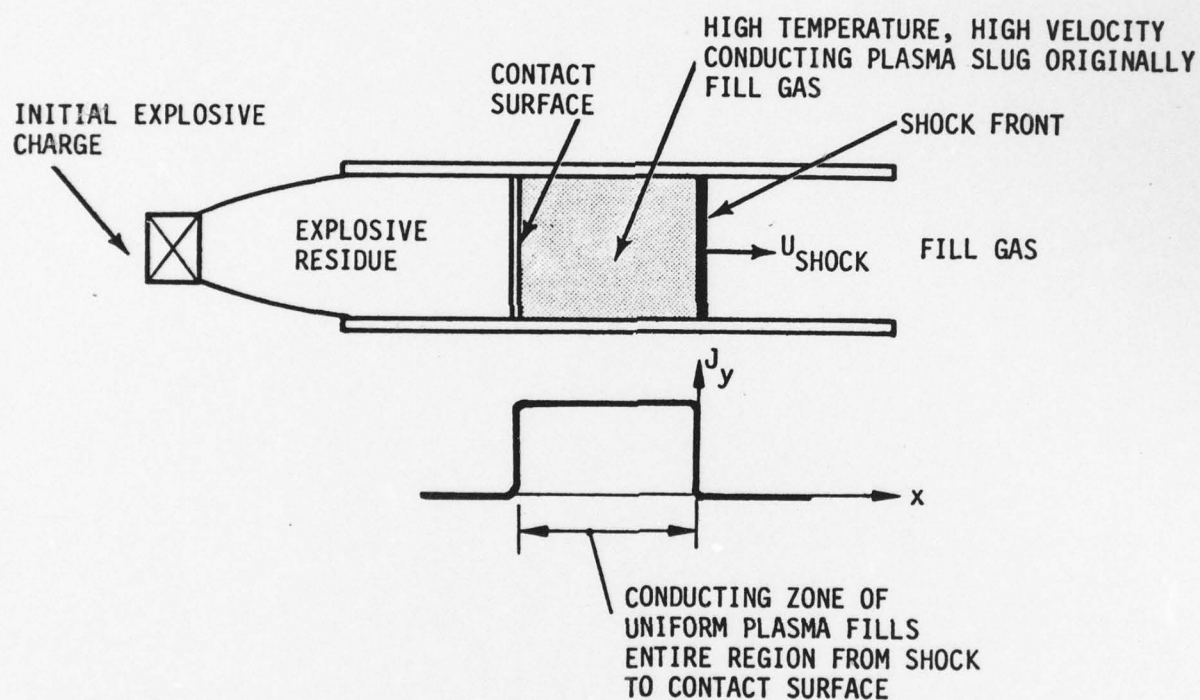
We consider two illustrations of such magnetogasdynamic non-uniformities. The first is for conventional explosion-driven MHD generators. Here we reveal the detailed structure of the deceleration of the conducting slug formed by the compression of plasma between the explosion-driven shock wave and its following contact surface. Such structure includes electrothermal and magnetic contraction of the current distribution within the slug and the corresponding nonuniform deceleration and Joule heating of the slug. The second illustration is for steady high Magnetic Reynolds Number channel flow. Here we exhibit the nonuniform manner in which the external magnetic field is diffused into the plasma and the corresponding nonuniform deceleration of the flow.

2. UNSTEADY FLOW: THE SHOCK TUBE MHD GENERATOR

2.1 Characterization of Nonuniformities

The idealized shock tube MHD generator [1] is shown in Fig. 2-1. An appropriately shaped chemical explosion charge is detonated into a gas which is compressed and heated behind the driven shock wave and the contact surface which separates the fill gas in the tube and the products of explosion. The high velocity conducting slug so formed passes through

DIRECT EXPLOSION DRIVEN MHD GENERATOR
IDEALIZED SYSTEM



8-2851

Fig. 2-1. Idealized shock tube MHD generator flow

the magnetic field generating a uniform current over its breadth [1], [9] and is uniformly decelerated.

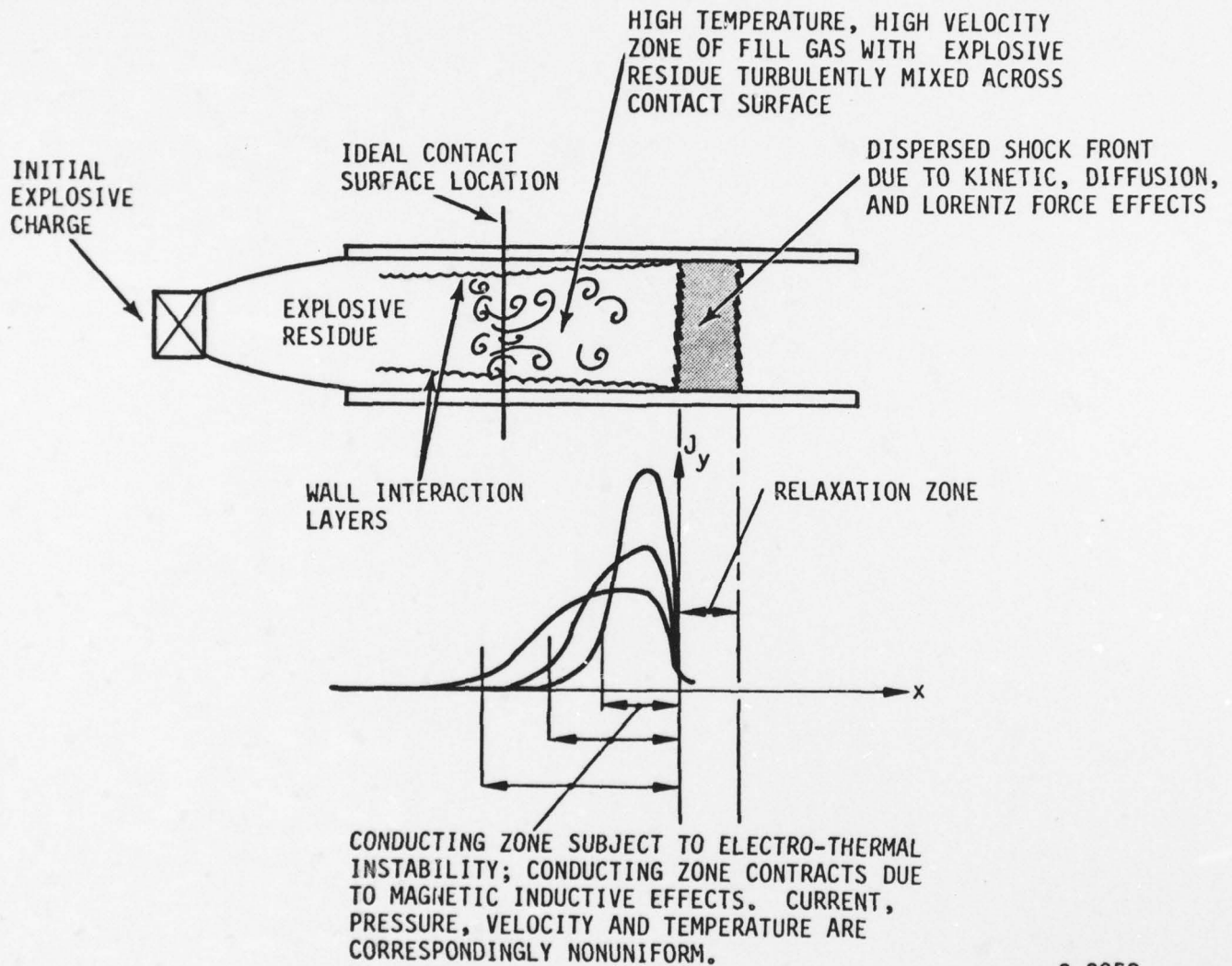
In Fig. 2-2, we exhibit some of the nonuniformities which will be present in such a flow. The shock front of the conducting zone will not be a sharply delimited region, but will in fact, be dispersed by two principal effects. First, kinetic-relaxation, radiative processes, and diffusively induced electric fields will smear the shock front [10], [11]. For conditions typical of chemical explosion drives, the shock front kinetic dispersion is of the order of 0.1-1.0 cm. [10],[11]. It is important to note, however, that careful consideration of all diffusional processes in a comprehensive Ohm's law [13] indicates significant effects which have not previously been considered. For example, Hall effects are normally neglected in such flows because of the high pressures involved; however, it is possible to show that the current induced by the diffusional term $\nabla p_e \times \vec{B}$ in the Ohm's law [13] is in the same direction as the generator current and for very strong shocks has the limiting value

$$J(\nabla p_e \times B) \sim e \frac{\omega_e}{Q_{ei}}$$

where e is the electronic charge, ω_e is the electron cyclotron frequency, and Q_{ei} is the electron-ion cross section. Such a current is of the order of 10^5 kA/m² and hence makes an important modification to the shock front of a *hydromagnetic* flow. The second dispersal mechanism for the slug front is the Lorentz force itself.

A second major nonuniformity in such a hydromagnetic flow is the nonuniformity induced in the current distribution by electrothermal heating and magnetic contraction. Since shock-generated conducting slugs in generators of length 0.1-1 m and applied magnetic fields of 1-10 T can be significantly Joule heated, the uniform discharge hypothesized for the ideal case of Fig. 2-1 is electrothermally and magneto-acoustically unstable as shown by Demetriades, et al.[14] and Oliver [15]. Hence, this electrothermally unstable discharge will contract either into one or several current

DIRECT EXPLOSION DRIVEN MHD GENERATOR
ELECTROMAGNETIC AND GASDYNAMIC NONUNIFORMITIES



8-2852

Fig. 2-2. Shock-tube MHD generator flow with fluid and electrical nonuniformities

concentrations or large scale 'arcs' depending upon the nature of initial nonuniformities present. We emphasize that electrothermal contraction is a phenomenon which can exist in low as well as high magnetic Reynolds number flows. In the case of high R_m flows however, another contraction mechanism is available which preferentially drives the current distribution to the front of the conducting slug. This is the hydromagnetic contraction effect which concentrates the current in a progressively thinner 'skin' at the slug front. Electrothermal contraction and magnetic contraction can of course, operate in concert. The net result is that in hydromagnetic flow in contrast to purely gasdynamic shock driven flow, the effective length of the conducting slug is not the region between the shock and the contact surface, but rather a hydromagnetic structure which has its own evolving internal nonuniformity.

A third class of nonuniformities are these associated with instability and mixing at the contact surface. Such anomolous mixing has been observed in both purely gasdynamic [16] and hydromagnetic flows. In the latter, the simplest observation is that alkali seed added to the explosive significantly affects generator performance. In the idealized generator of Fig.2-1 such material cannot exist in the conducting zone.

Lastly, we mention wall effects which include boundary layers developing behind the shock (are they truly laminar in the hydromagnetic case as evidence seems to suggest for purely gasdynamic shocked flow [17]?) and local small scale arc-mode transport at the electrode surfaces.

2.2 Mathematical Description

We consider a quasi-one-dimensional description of a fluid moving in the spatial coordinate x and unsteady in time t . Average properties (over the cross section) of the duct describing the flow are its density ρ , internal energy e , velocity u , pressure p , and species mass compositional fraction c_α ($\alpha = 1, 2, \dots, n$). From these we select the total mass, momentum, energy densities $[\rho, m = \rho u, e = \rho(e + u^2/2)]$, as the state $\underline{U}(x, t)$ specifying the flow at any point in space and time:

$$\underline{U}(x,t) = \begin{bmatrix} \rho \\ m \\ e \end{bmatrix} . \quad (2.1)$$

The state \underline{U} is augmented with the compositional vector c_α . The fluid conservation laws are

$$\partial_t \underline{U} = -\partial_x \underline{F} + \partial_x (\epsilon \partial_x \underline{U}) + \underline{S} - \underline{D} \quad (2.2a)$$

$$\partial_t c_\alpha + u \partial_x c_\alpha = \partial_x (\epsilon \partial_x c_\alpha) + \dot{c}_\alpha \quad (2.2b)$$

In the above, \underline{F} represents the convected fluxes of mass, momentum, and energy, \underline{S} and \underline{D} are the Lorentz and wall loss vectors, ϵ represents a diffusion coefficient characterizing the mixing processes in the region of the contact surface, and \dot{c}_α is the chemical source term for species α . In terms of the current density \vec{J} , electric field \vec{E} , and magnetic field \vec{B} , the Lorentz vector is

$$\underline{S} = \begin{bmatrix} 0 \\ (\vec{J} \times \vec{B})_x \\ \vec{J} \cdot \vec{E} \end{bmatrix} \quad (2.3)$$

The loss vector D has the form

$$D = \frac{4}{D_H} \begin{bmatrix} m \frac{d\delta^*}{dx_s} \\ \tau_w \\ q_w \end{bmatrix} \quad (2.4)$$

where $\frac{d\delta^*}{dx_s}$ is the rate of change of displacement thickness of the boundary layer with respect to shock coordinates, and τ_w , q_w are the wall shear stress and heat flux, respectively.

In the illustration study we assume that the kinetic effects are confined to the relaxation layer at the shock [we do not consider here such phenomena as photoionization and gas breakdown in regions adjacent to the shock [10], [11], [12] which can occur under some conditions.] Further, for the illustrations to be presented, we assume this relaxation layer is thin compared to the overall thickness of the conducting zone.

The electromagnetic effects are described by the Maxwell equations

$$\nabla \times \vec{B} = \mu_0 \vec{J} \quad \partial_t \vec{B} = -\nabla \times \vec{E} \quad (2.5)$$

and the Ohm's law which outside the region of intense gradients assumes the form

$$\vec{J} = \sigma(\vec{E} + \vec{u} \times \vec{B}) \quad (2.6)$$

with $\sigma = \sigma(p, T, c_\alpha)$. The forms of Eq. (2.5) allow representation of \vec{E} and \vec{B} in terms of scalar potential Φ and vector potential \vec{A} as

$$\begin{aligned} \vec{E} &= -\nabla \Phi - \partial_t \vec{A} \\ \vec{B} &= \nabla \times \vec{A} \end{aligned} \quad (2.7)$$

For the simple geometry of magnetic field in the z direction and continuous electrodes perpendicular to the y axis, the electrical equations reduce to

$$\begin{aligned} E_y &= -\frac{(V-V_d)}{h} - \partial_t A_y \\ B_z &= \partial_x A_y \\ J_y &= \sigma(E_y - u B_z) = -\mu_0^{-1} \partial_x B_z \\ \partial_t A_y + u \partial_x A_y &= \eta \partial_x \partial_x A_y - \frac{(V-V_d)}{h} \end{aligned} \quad (2.8)$$

In the above, V is a uniform voltage over the range of the continuous electrodes and V_d is the voltage drop through boundary layers.

Since the characteristic electric field in the MHD flow is of the order $\vec{u} \times \vec{B}$ we may estimate the importance of the inductive term $\partial_t \vec{A}$ relative to $\vec{u} \times \vec{B}$. The term $\partial_t \vec{A}$ is of the order $B_i u$ where B_i is the field induced by the plasma currents. From the last of Eqs. (2.8) we find $B_i \sim (1-K) R_m B_z$ and $\nabla \Phi \sim Ku B_z$ where $R_m = \mu_0 \sigma u a$ is the Magnetic Reynolds Number and a is the characteristic length of the conducting zone. Hence we find $|\partial_t \vec{A}|$ is of order $(1-K) R_m |\vec{u} \times \vec{B}|$. Thus, self-induction effects in the plasma must be included for $(1-K) R_m \gtrsim 1$.

The electrical equations (2.8) require closure with an external loading condition. If we integrate the last of Eqs. (2.8) in x over the electrode extent, we obtain the total current as

$$I = -A \left[\langle \sigma \rangle \frac{(V-V_d)}{h} + \langle \sigma u B_z \rangle \right] - A \langle \sigma \partial_t A_y \rangle \quad (2.9)$$

where A is the electrode area and $\langle \rangle$ indicates an average over the length of the electrodes. Defining the internal resistance of the generator as $R_i \equiv h/(A \langle \sigma \rangle)$ and the Faraday voltage V_F as $V_F \equiv h \langle \sigma u B_z \rangle / \langle \sigma \rangle$ we may express Eq. (2.9) as

$$\frac{h}{\langle \sigma \rangle} \langle \sigma \partial_t A_y \rangle + IR_i = -(V-V_d) - V_F. \quad (2.10)$$

The external circuit equation is

$$L_e \frac{dI}{dt} + R_L I = V \quad (2.11)$$

where R_L and L_e are the load resistance and external circuit inductance respectively. Eqs. (2.10) and (2.11) govern the evolution of the global generator current I and voltage V .

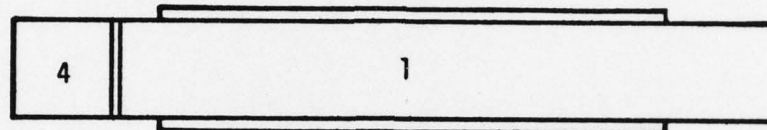
2.3 Flow Structure Prediction in a Shock Tube Generator

We now turn to an application of the foregoing mathematical description to a typical shock tube MHD generator. We consider a generator of approximately 1 m length and 2.5 cm cross section dimension whose explosive charge is an RDX composition detonating into residual explosion products [2]. The initial and operating conditions for this machine are given in Table 2-1. The initial condition for the simulation is taken as that of fully detonated explosion products at detonation pressure and temperature occupying a volume negligibly different from that of their nondetonated state (Region 4) and residual explosion products at 300°K and 10 Torr pressure (Region 1).

In the interest of minimizing costs in this initial study, simplified thermodynamic and electrical conductivity functions were utilized rather than the comprehensive real gas thermochemical and electrical conductivity algorithm in the STD Research codes. These consisted of a parameterized specific heat ratio γ which reflected the reactive nature of the residual explosion products ($\gamma \approx 1.17$) and simple conductivity functions allowing for a singly ionized species interacting with a neutral background (three component plasma). Since significant multiple ionization is likely in these plasmas, the simplified functions are probably not accurate above about 20,000°K. Above 20,000°K, this simplified conductivity is suppressed by the upper limit on electron number density imposed by the restriction to a singly ionized species. This conductivity function will underlie the structure of some of the results we will now describe.

Since the computational simulation may be executed with or without the effect of induced magnetic field, we will examine the differences between flows which are allowed to generate an induced magnetic field and those which are not. In the first sequence of results in Figs. 2-3a through 2-3d and Figs. 2-4a through 2-4c, the flow is not permitted to experience the effects of an induced magnetic field. In Figs. 2-3 we observe the evolution of the flow in the x-t plane with the amplitude of the various

TABLE 2-1
Nominal Conditions for Shock Tube
MHD Generator (Ref. [2])



Explosion products in zone 4, at
pressure p_4 , temperature T_4 at time $t = 0$.
Fill gas (residual products) in zone 1 at
pressure p_1 , temperature T_1

p_4/p_1	2.2×10^7
T_4/T_1	17
$u_{\text{shock ideal}}$	8236 m/s
$M_{\text{shock ideal}}$	27
B_0	1 Tesla
D_{tube}	2.54 cm
$L_{\text{electrodes}}$	86 cm
Load Impedance	4×10^{-3} ohm
2% potassium seed in fill gas	

8-2853

F = -JY, AMPS/SD.M
 X = AXIAL DISTANCE, M
 T = TIME, SEC.
 X MIN = 0.
 X MAX = 1.15E+00
 T MIN = 1.29E-06
 T MAX = 1.50E-04
 F MIN = -2.66E+06
 F MAX = 1.91E+07

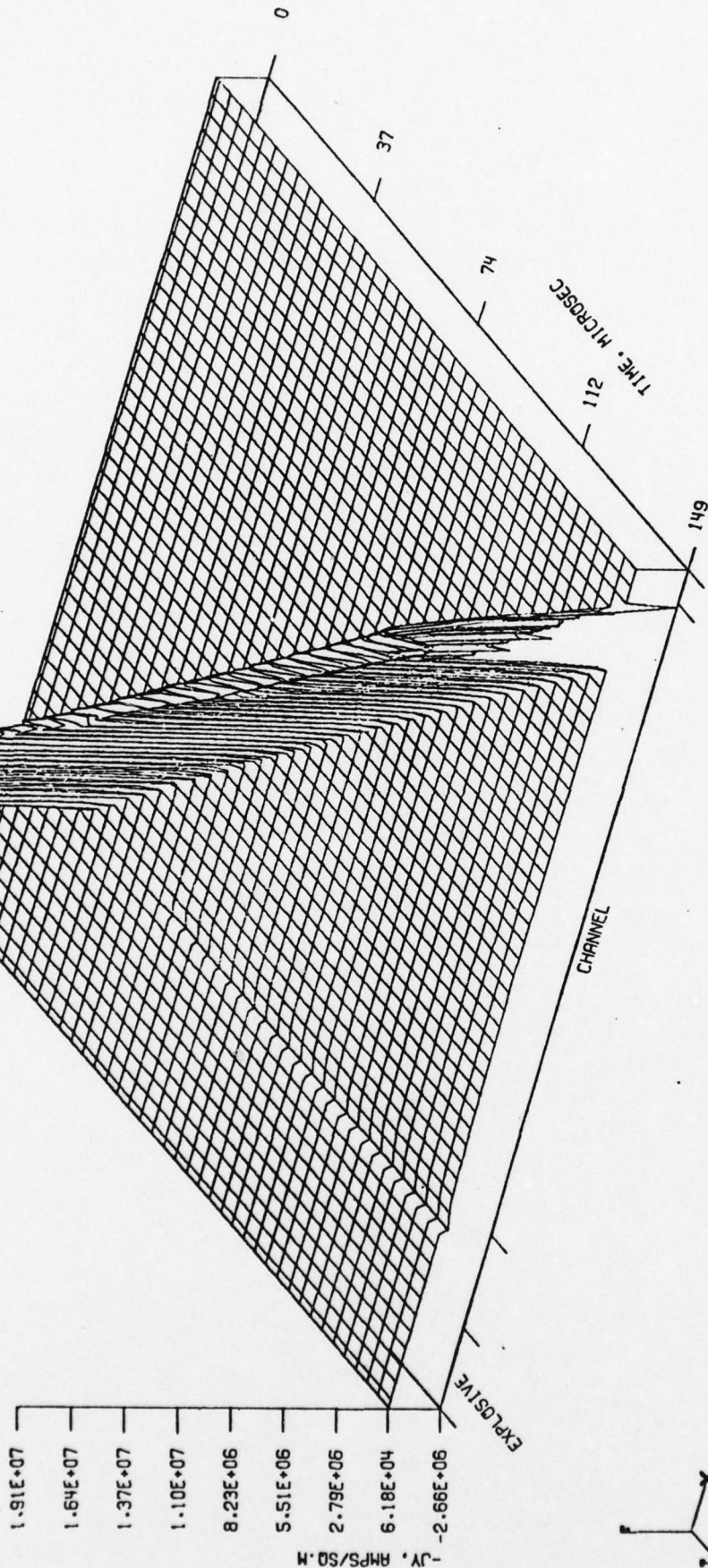


Fig. 2-3a. Evolution of current distribution in shock tube MHD generator for conditions of Table 2-1. Induced magnetic field suppressed. Note growing electrothermal instability in slug consisting of current concentration at front and rear of slug

8-2854

$F = \text{LOG}(\text{PRESSURE})$
 $X = \text{AXIAL DISTANCE, M}$
 $T = \text{TIME, SEC.}$
 $X \text{ MIN} = 0.$
 $X \text{ MAX} = 8.11\text{E-}01$
 $T \text{ MIN} = 0.$
 $T \text{ MAX} = 1.48\text{E-}04$
 $F \text{ MIN} = 2.43\text{E+}00$
 $F \text{ MAX} = 9.78\text{E+}00$

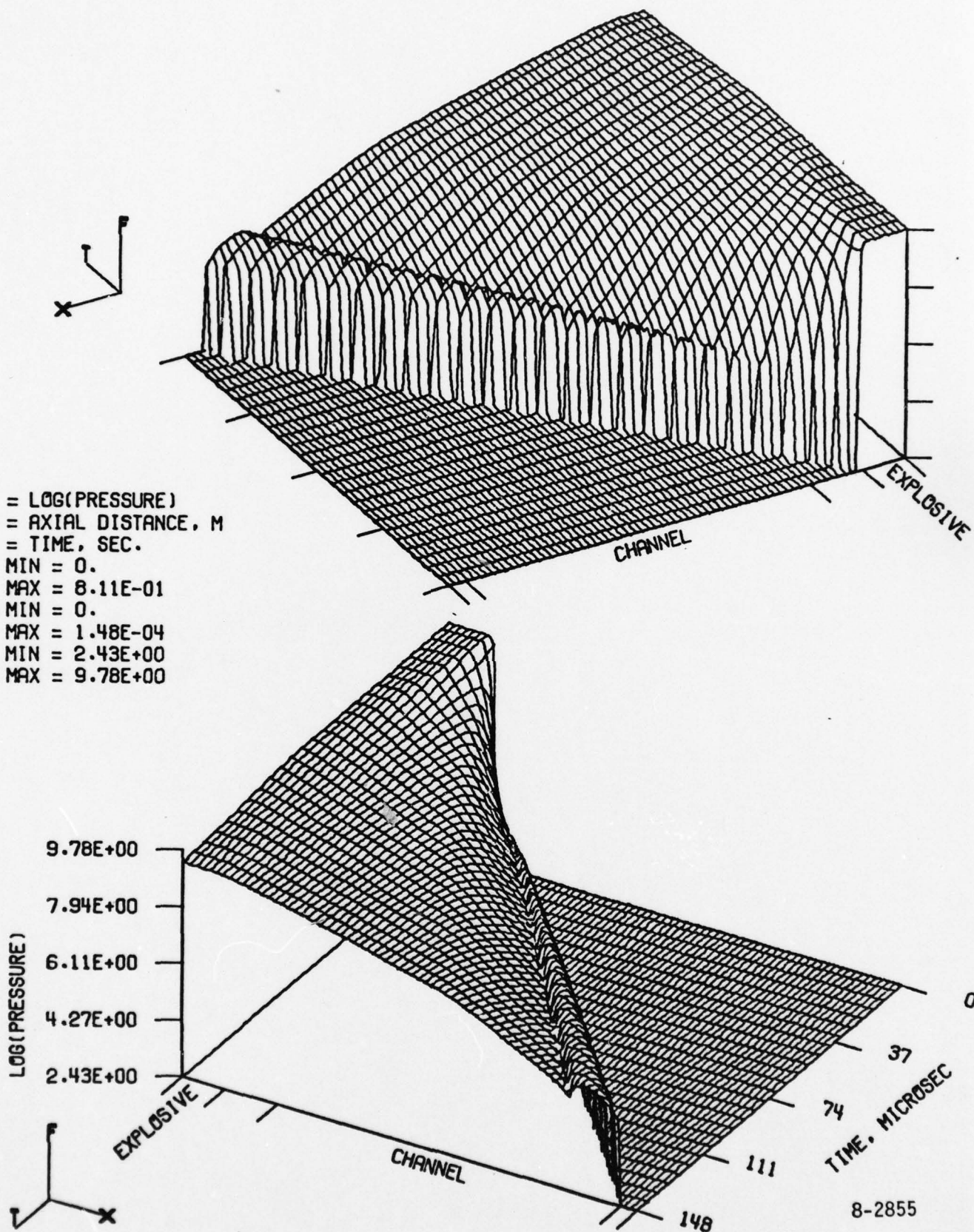


Fig. 2-3b. Pressure evolution for conditions of Fig. 2-3a. Note increased pressure inside conducting slug due to decelerating Lorentz force

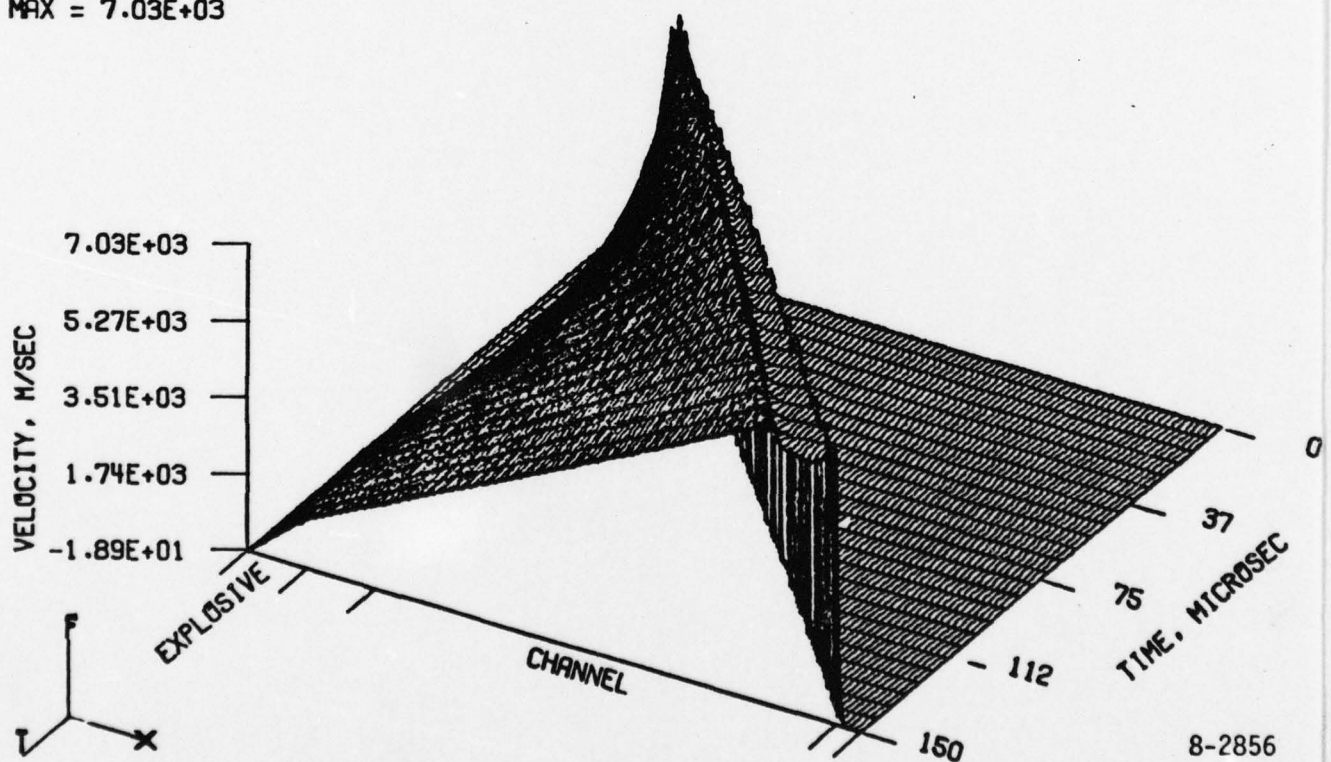
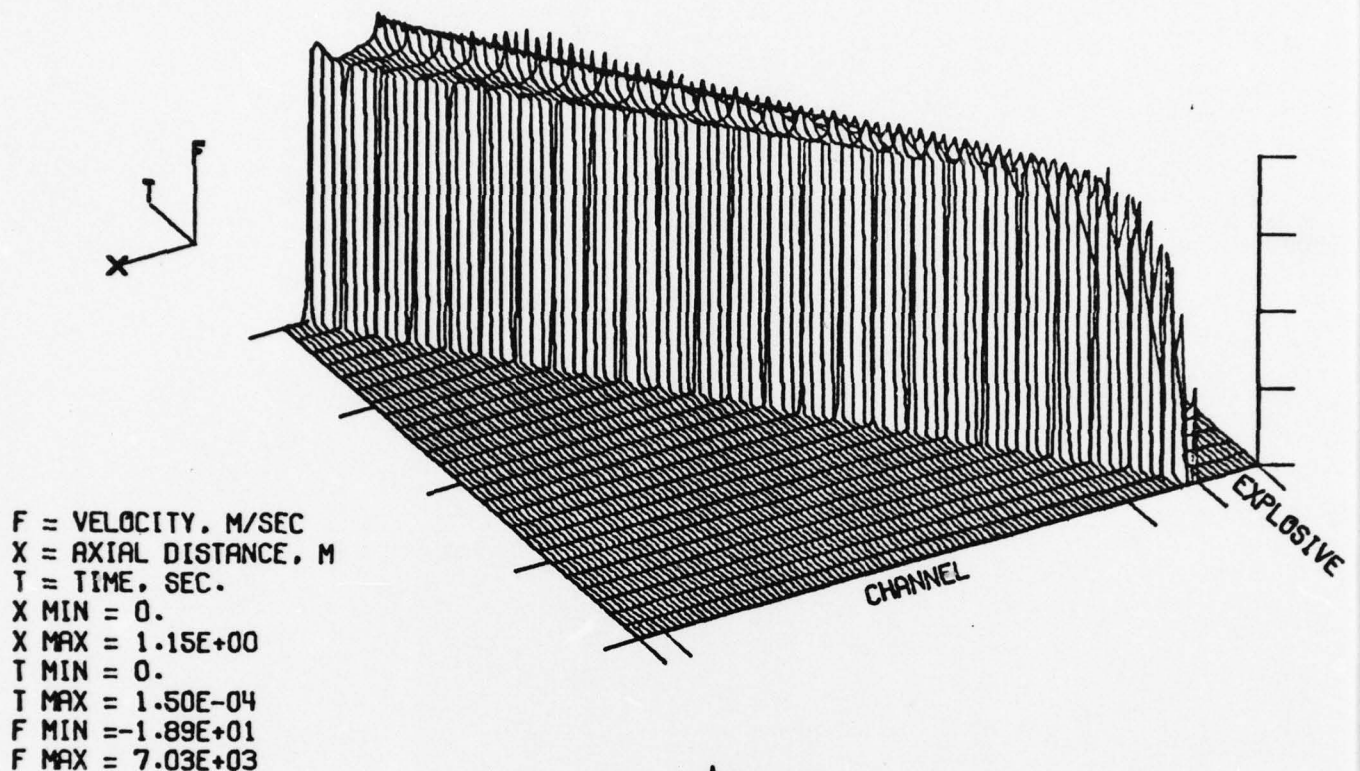


Fig. 2-3c. Velocity evolution for conditions of Fig. 2-3a. Note maximum deceleration in center of slug and velocity "overshoots" at slug edges

8-2856

F = TEMPERATURE, K
 X = AXIAL DISTANCE, M
 T = TIME, SEC.
 X MIN = 0.
 X MAX = 1.15E+00
 T MIN = 1.29E-06
 T MAX = 1.50E-04
 F MIN = 3.00E+02
 F MAX = 7.06E+04

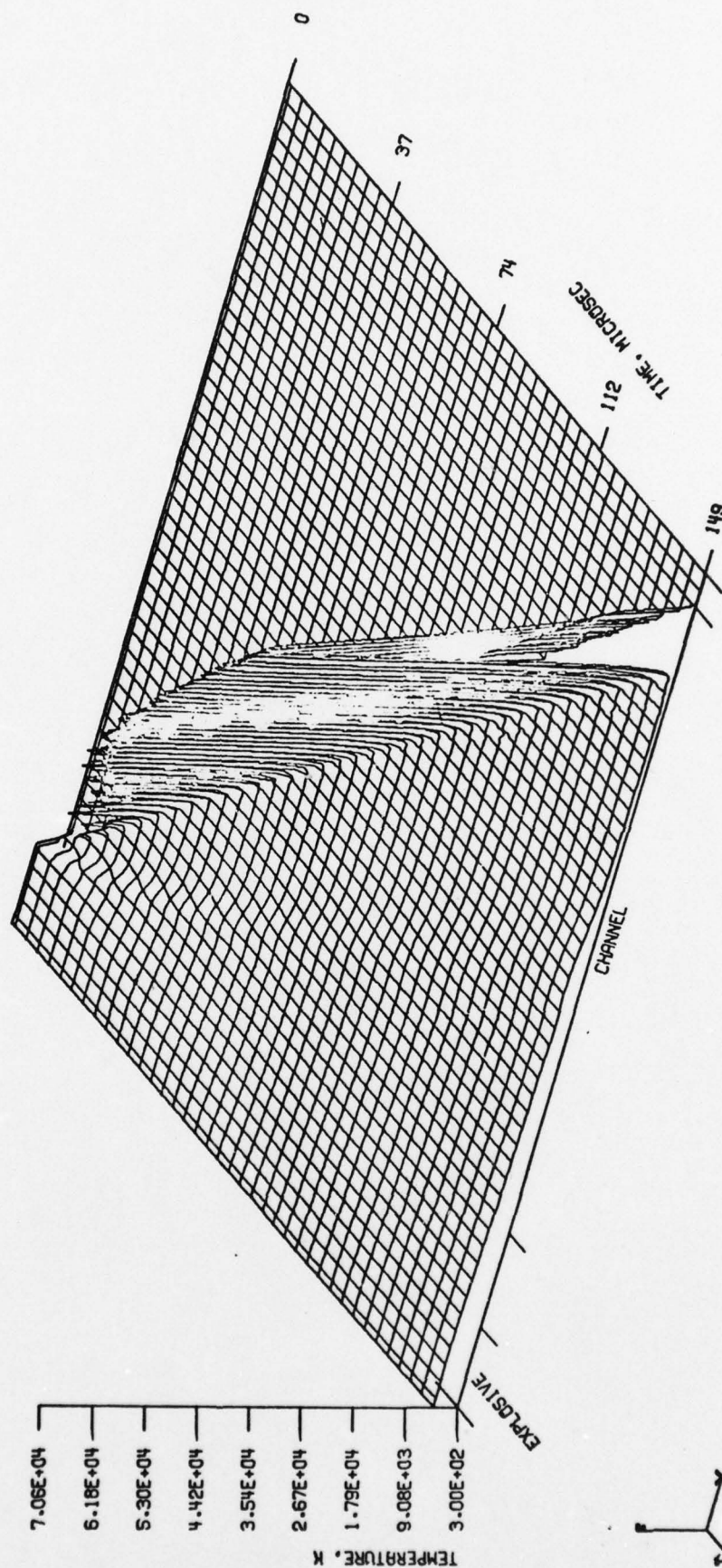
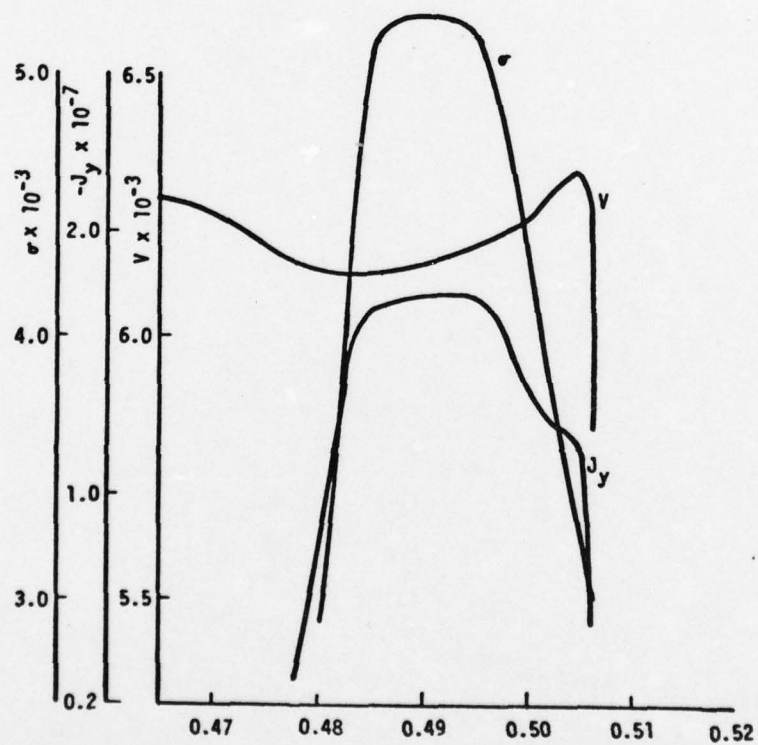
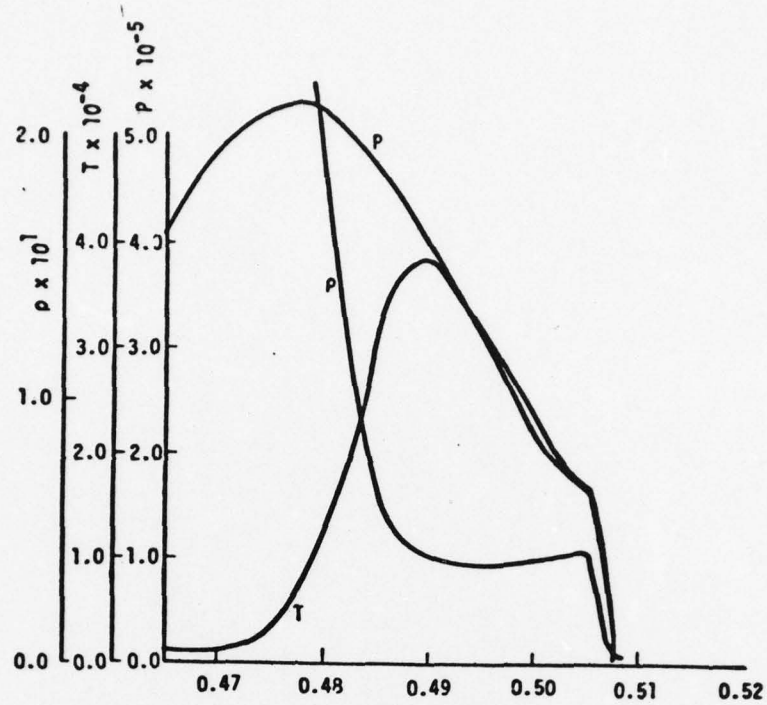


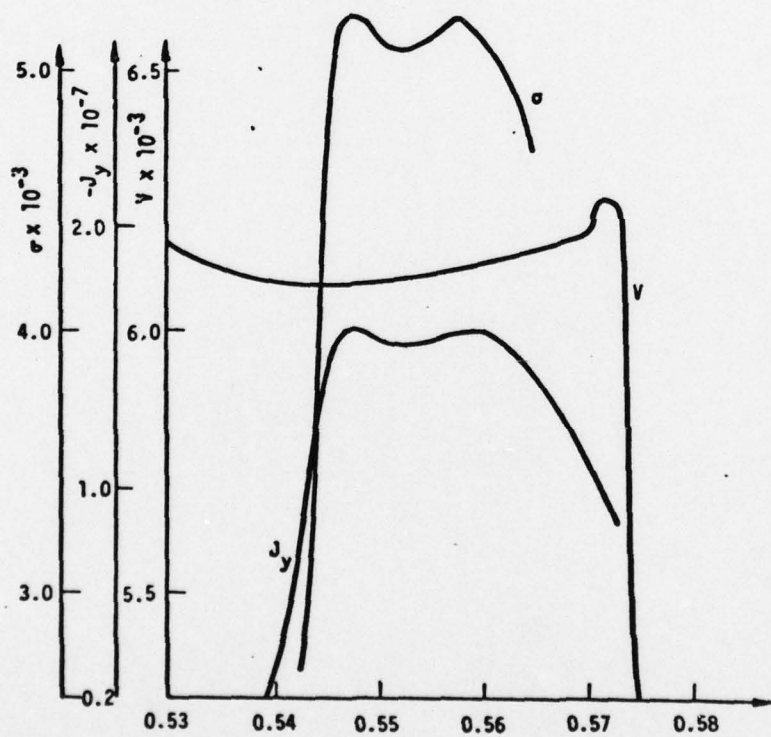
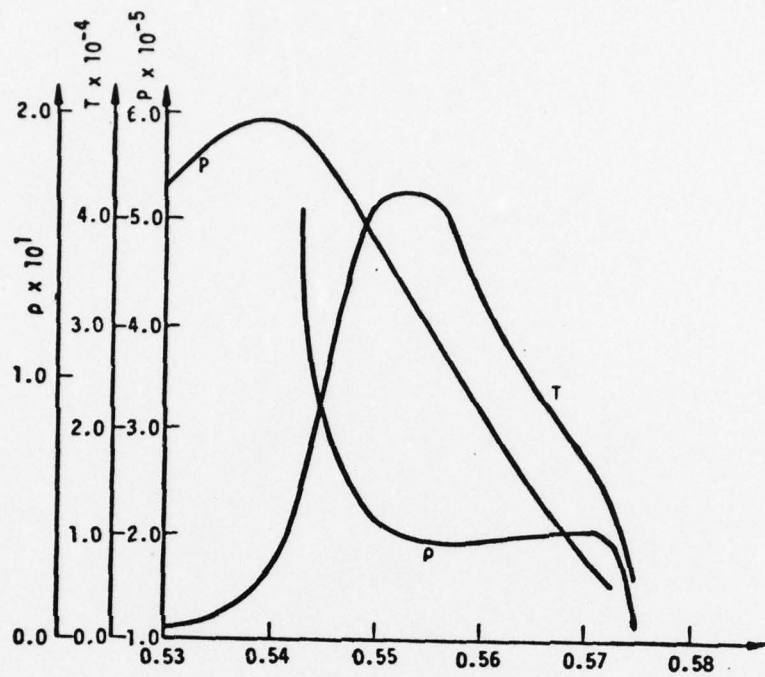
Fig. 2-3d. Temperature evolution for conditions of Fig. 2-3a.
 Note growing temperatures over the course of
 evolution due to Joule heating of the conducting slug

8-2857



8-2858

Fig. 2-4a. Detailed distribution of fluid and electrical variables through the high velocity, high temperature region for the evolution in Figs. 2-3. $t = 50 \mu s$



8-2859

Fig. 2-4b. Detailed distribution of fluid and electrical variables through the high velocity, high temperature region for the evolution in Figs. 2-3. $t = 70 \mu s$

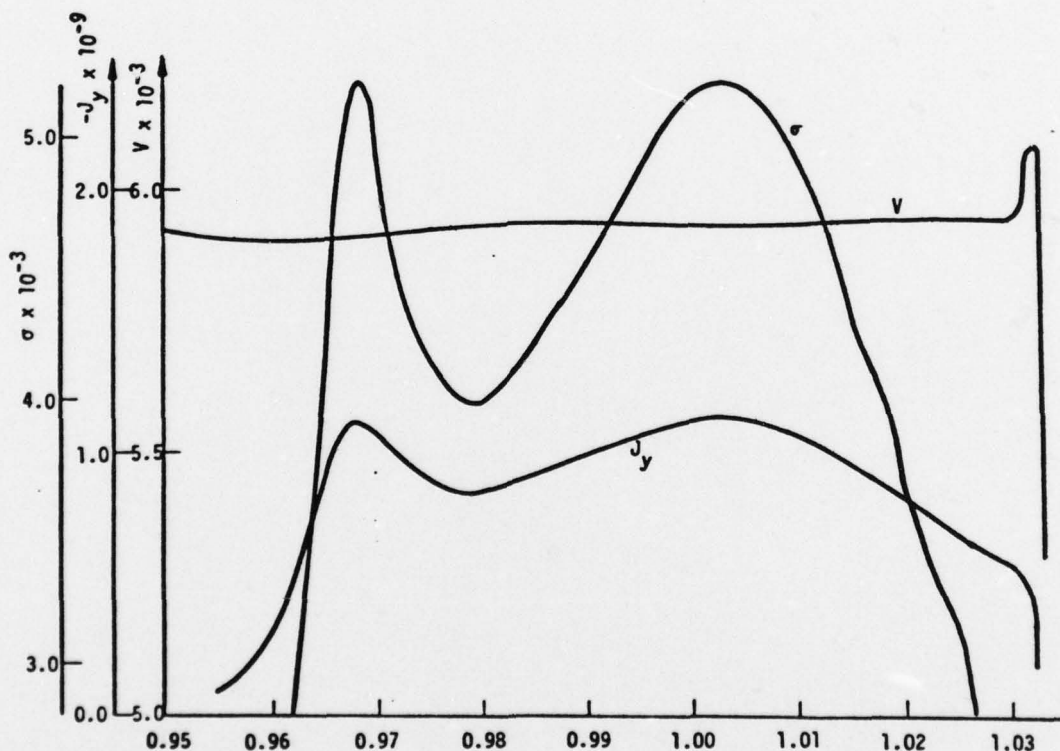
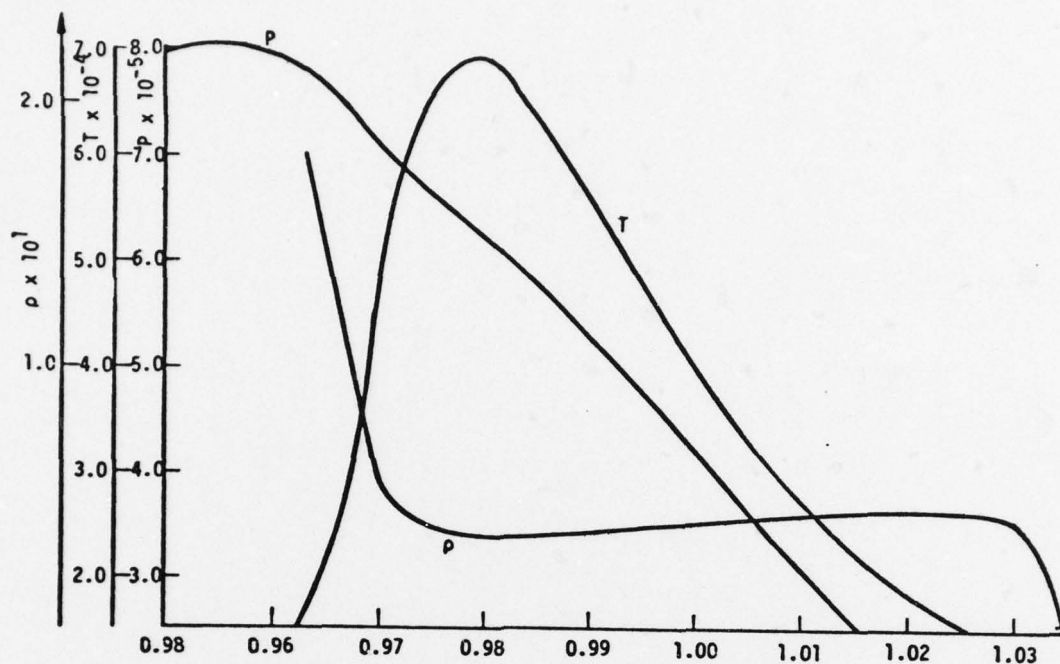


Fig. 2-4c. Detailed distribution of fluid and electrical variables through the high velocity, high temperature region for the evolution in Figs. 2-3, $t = 140 \mu s$. Note "double-humped" electrothermal instability due to single-ionization conductivity law. Full real gas effects would likely lead to only a "one-humped" instability.

8-2860

fluid and electrical variables displayed. In Figs. 2-4 we observe the same situation, but in expanded scale so as to observe the flow structure present. At about 20 μ s the conducting slug enters the generator and produces the current pulse which propagates through and out of the generator by about 160 μ s. The overall length of the slug grows, but the current distribution within the slug has its own evolving internal structure. Because of the decelerating Lorentz forces, the pressure within the slug is actually increased over that for a non-MHD flow and an expansion wave follows the slug as shown in Fig. 2-3b. Similarly, the velocity within the slug is decelerated below that at the leading and trailing edges of the slug leading to velocity "overshoots" at the leading and trailing edges. (Fig. 2-3c). In Fig. 2-3d it can be seen that there is a significant growth in the average temperature levels within the slug due to the Joule heating present (the reader should bear in mind that the actual temperature levels must be considered approximate due to the use of simplified thermodynamic functions). In Fig. 2-3a and Fig. 2-4a it can be seen that during the course of its evolution a growing nonuniform current concentration is present. This is because in the range of temperatures below 20,000°K (for the simplified conductivity model) the plasma is electrothermally unstable [14],[15] and the initial nonuniformity present in the slug shape is growing. Once the temperatures exceed 20,000°K in the center of the slug, the central region actually becomes electrothermally stable (because the simplified conductivity functions have the property $\partial\sigma/\partial T < 0$ in this region). Since only the edges of the slug are unstable, these edge regions grow and we see a "double-humped" growing instability. In Figs. 2-5 and 2-6 we see the same pulse evolution but for higher interaction corresponding to $B_0 = 3$ Tesla. Here, the electrothermally unstable slug has evolved greater nonuniformities.

For real gases in which $\partial\sigma/\partial T$ is a principally positive function over the entire range of temperatures and pressures encountered, the electrothermal instability will likely evolve as a single growing, contracting, intensifying nonuniformity.

$F = -J_Y$, AMPS/SQ.M
 $X =$ AXIAL DISTANCE, M
 $T =$ TIME, SEC.
 $X_{MIN} = 0$
 $X_{MAX} = 1.15E+00$
 $T_{MIN} = 1.29E-06$
 $T_{MAX} = 9.60E-05$
 $F_{MIN} = -2.06E+06$
 $F_{MAX} = 2.44E+07$

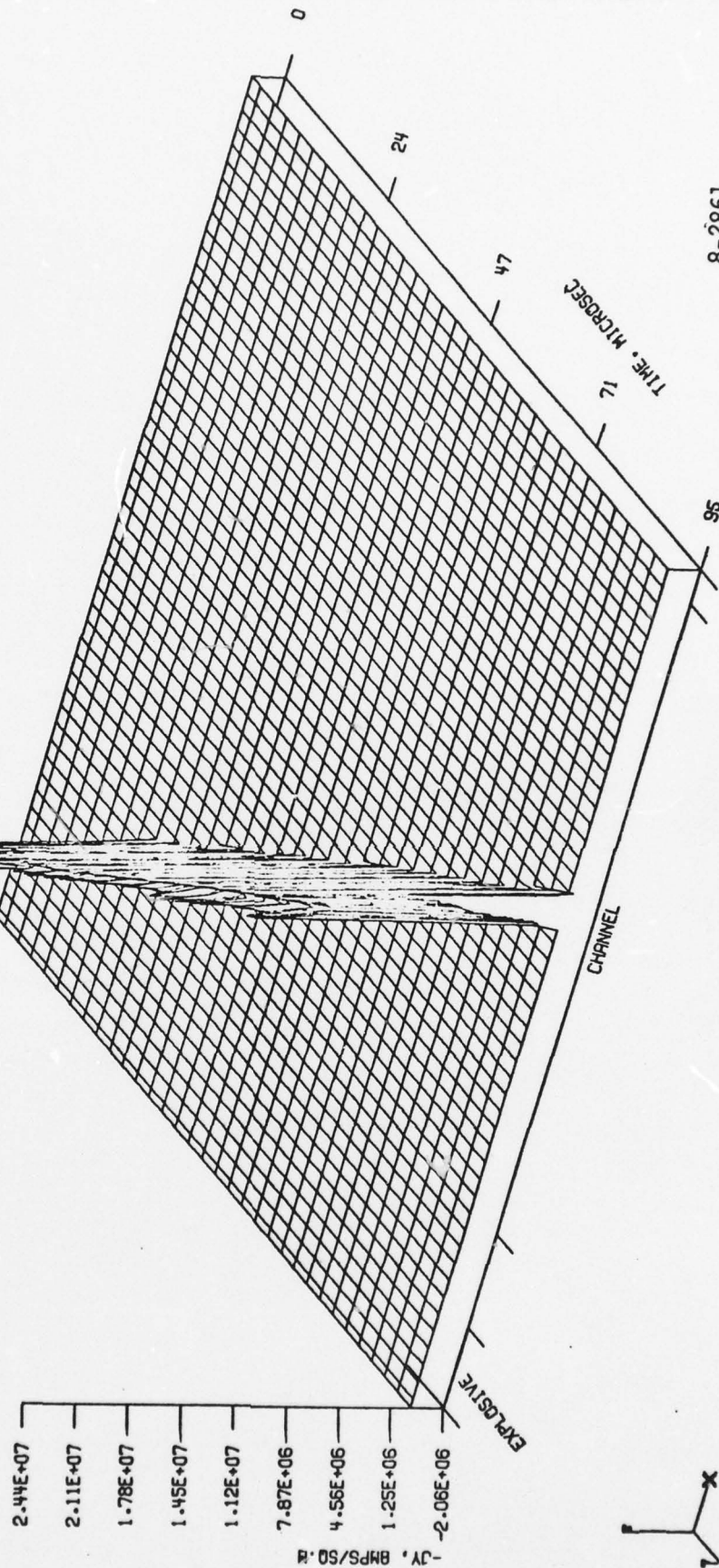


Fig. 2-5a. Current evolution for high interaction case. $B_0 = 3$ Tesla;
 all other conditions as in Figs. 2-3. Note enhanced
 deceleration and intensified nonuniformity

8-2861

F = VELOCITY, M/SEC
 X = AXIAL DISTANCE, M
 T = TIME, SEC.
 X MIN = 0.
 X MAX = 1.15E+00
 T MIN = 1.29E-06
 T MAX = 9.60E-05
 F MIN = -1.75E+01
 F MAX = 7.03E+03

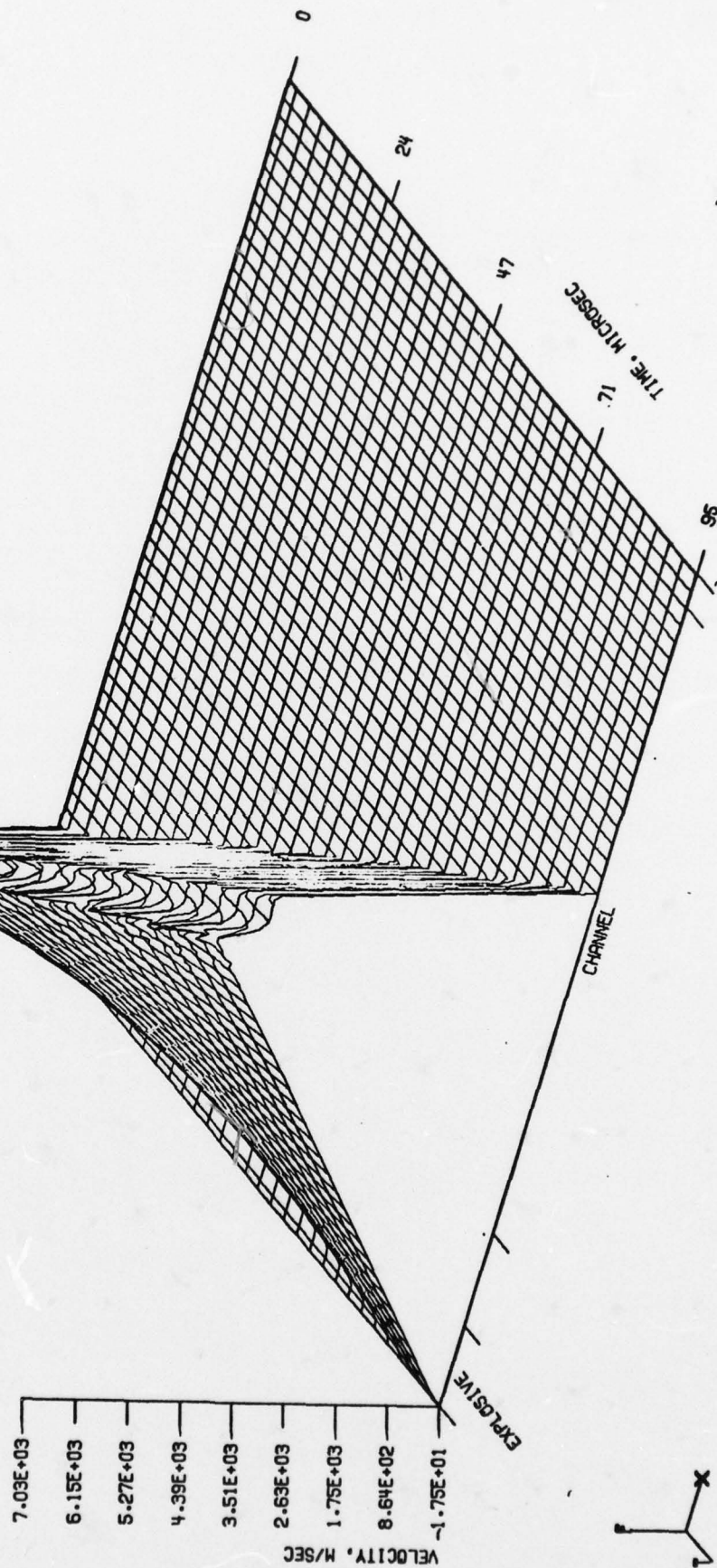
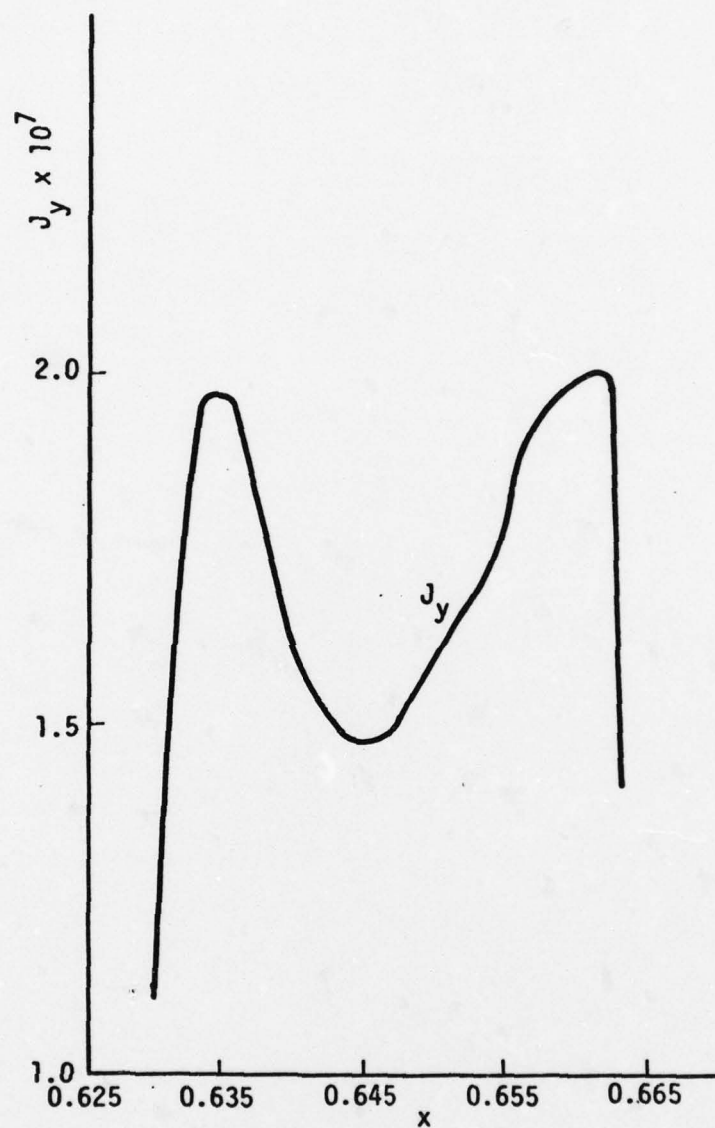


Fig. 2-5b. Velocity evolution for $B_0 = 3$ Tesla case in Fig. 2-5a

8-2862



8-2863

Fig. 2-6. Detailed distribution of current for $B_0 = 3$ Tesla case in Fig. 2-5a, $t = 90 \mu s$

In Figs. 2-7 and 2-8 we see the same case shown in Figs. 2-3 and 2-4 but with full inclusion of induced magnetic field effects. The interaction is somewhat higher in this case and because of the hydro-magnetic contraction of the current, the rear instability has been diminished and the leading edge instability has been enhanced and driven to the front of the slug (Figs. 2-7a, 2-8a). The signature of the induced field can be seen in Fig. 2-7b where the conducting slug has evolved a 1.48 Tesla field ahead and an 0.52 Tesla field behind. For these conditions $R_m \approx 0.5$.

In Fig. 2-9 we see the evolution of the total current and total energy produced in the run. Notice that at this $4 \times 10^{-3} \Omega$ loading condition the maximum current is reached near the end of the run. This is because the current density levels in the plasma rise with time due to Joule heating and axial growth of the slug. The $4 \times 10^{-3} \Omega$ loading is perhaps closer to short circuit rather than open circuit for these conditions which correspond to those of [9]. Closer to open circuit, one would expect less Joule heating and the maximum current point would occur midway in the pulse. Closer to short circuit the maximum current would occur near the end of the pulse. In Figs. 2-10 we display some of the experimental results for these conditions from [9]. It can be seen that the shift of the current maximum to the late-time portion of the run seems to correlate with the degree of loading.

F = -JY, AMPS/SQ.M
 X = AXIAL DISTANCE, M
 T = TIME, SEC.
 X MIN = 0.
 X MAX = 1.15E+00
 T MIN = 1.29E-06
 T MAX = 1.54E-04
 F MIN = -0.
 F MAX = 1.96E+07

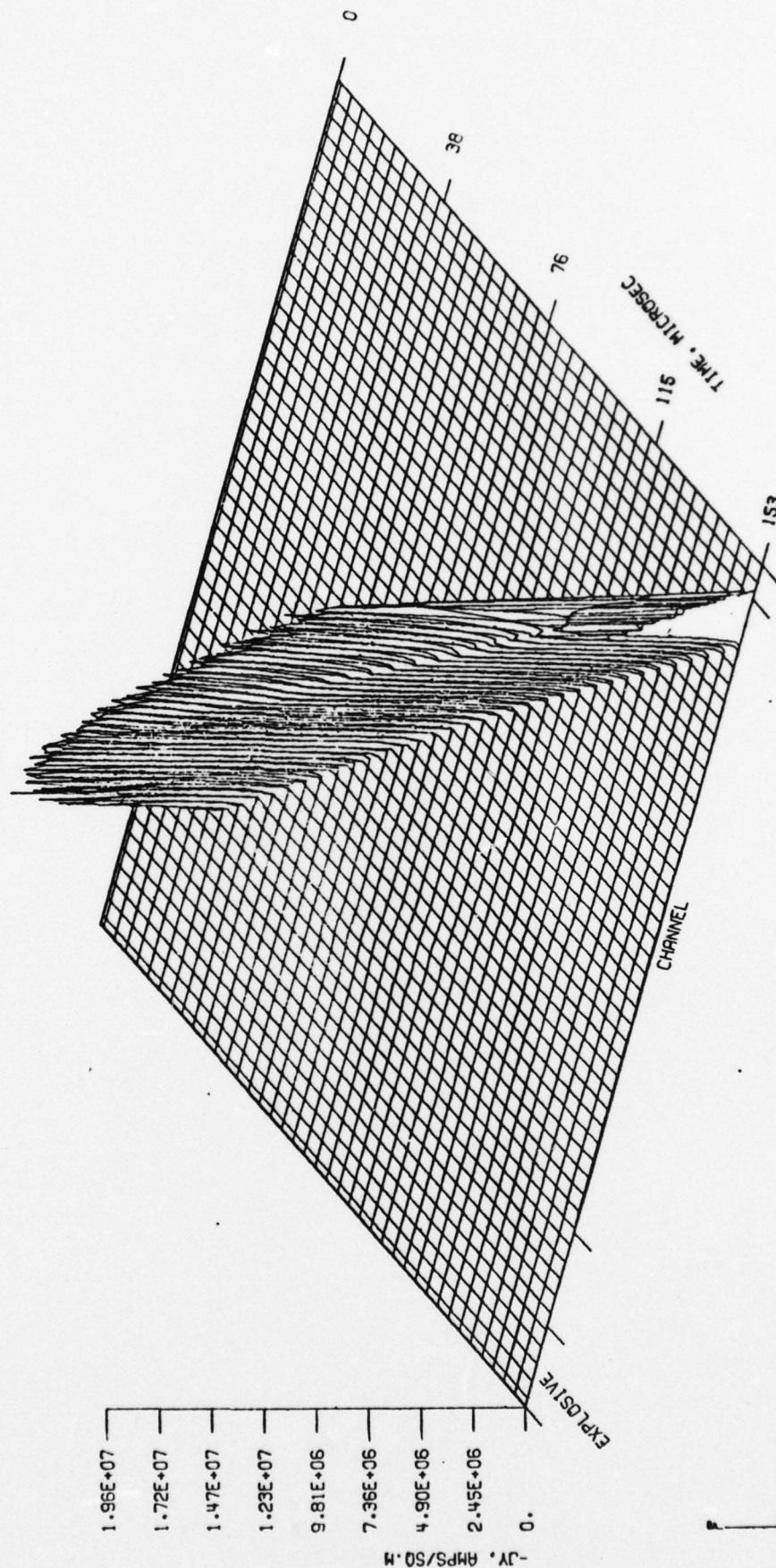


Fig. 2-7a. Evolution of the current distribution for the case shown in Figs. 2-3 and 2-4 but with induced magnetic field effects included. Note how inductive effects have concentrated the electrothermal instability at the front of the conducting slug. (See also Fig. 2-8)

8-2864

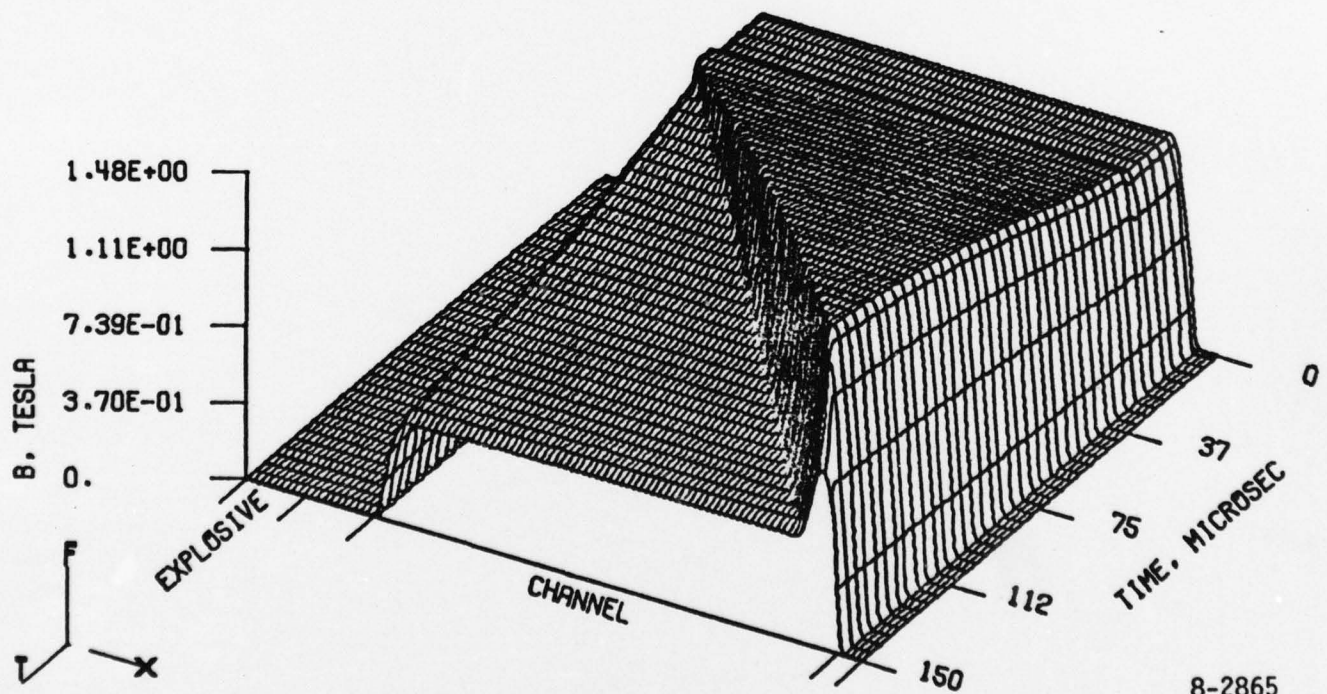
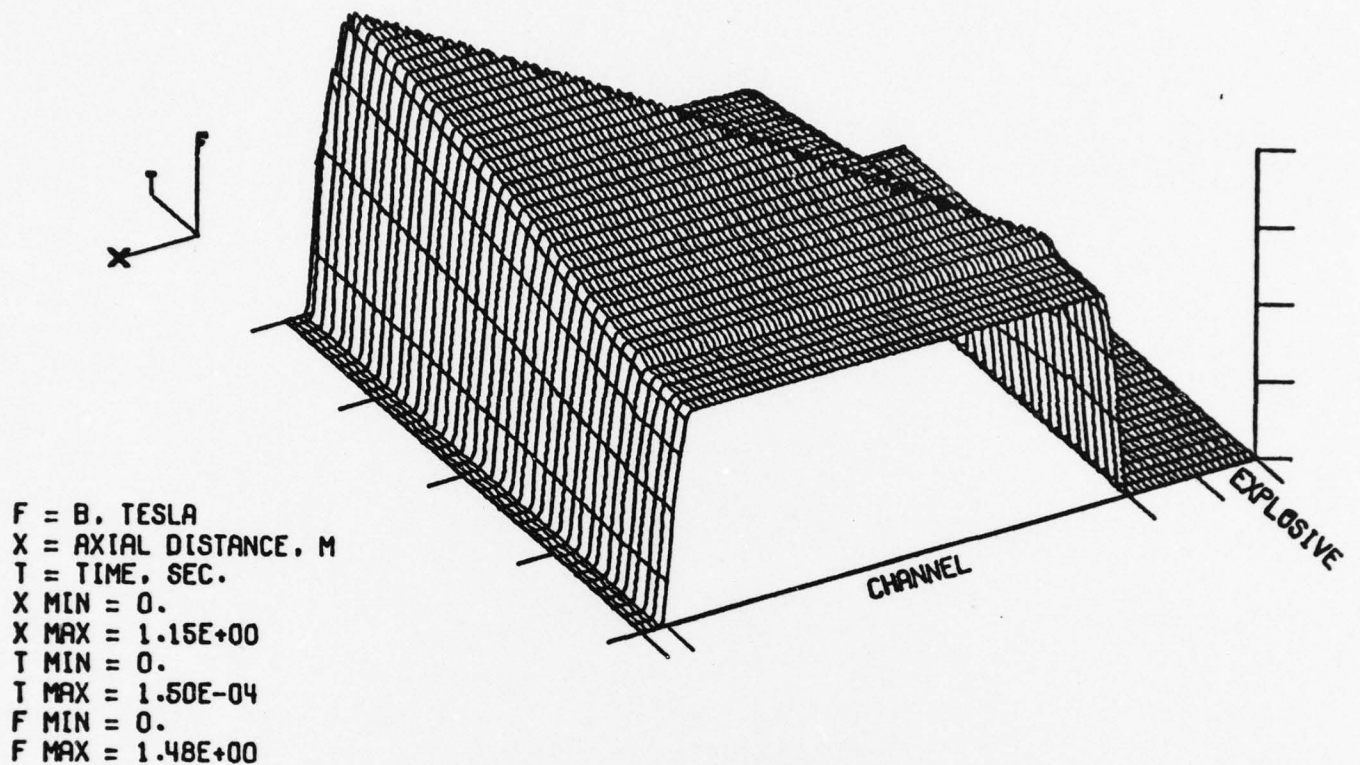
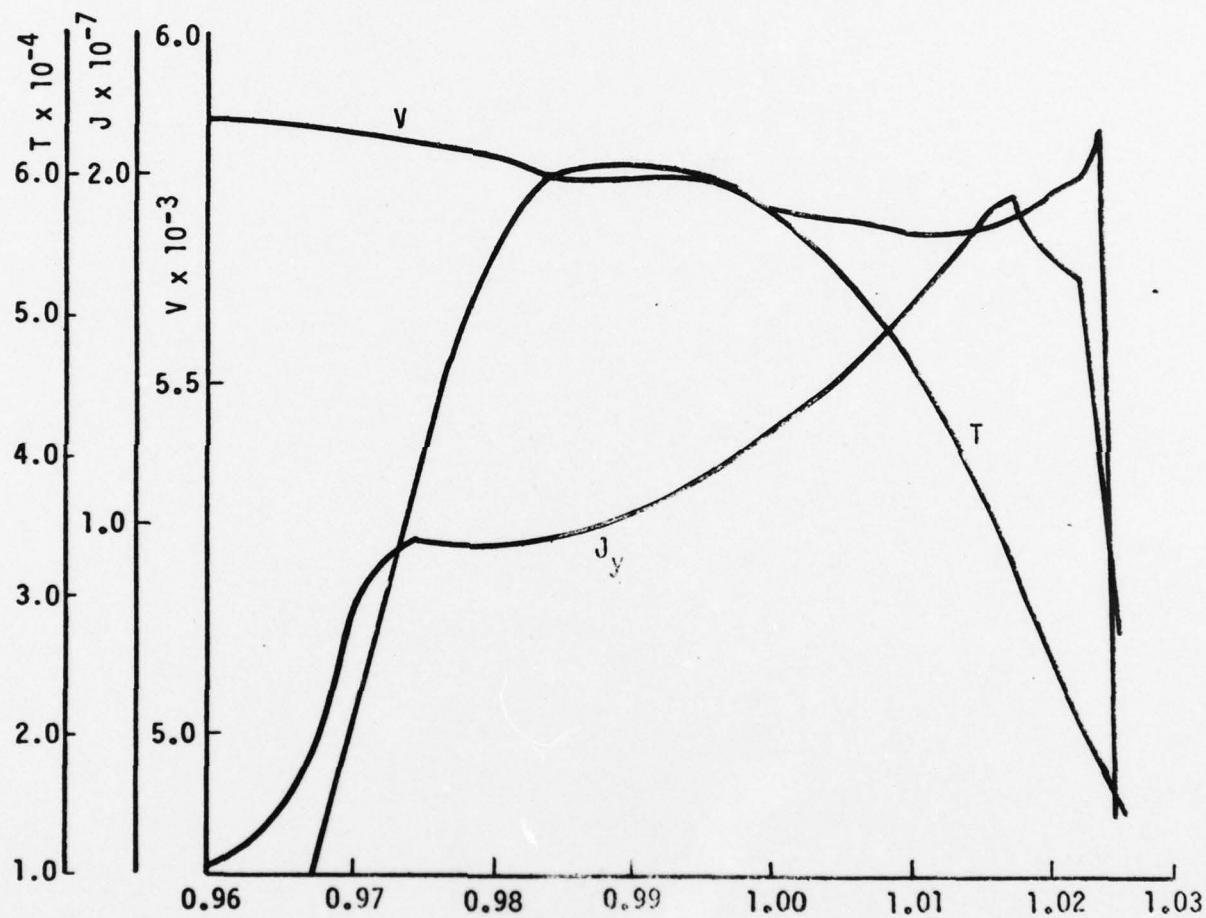


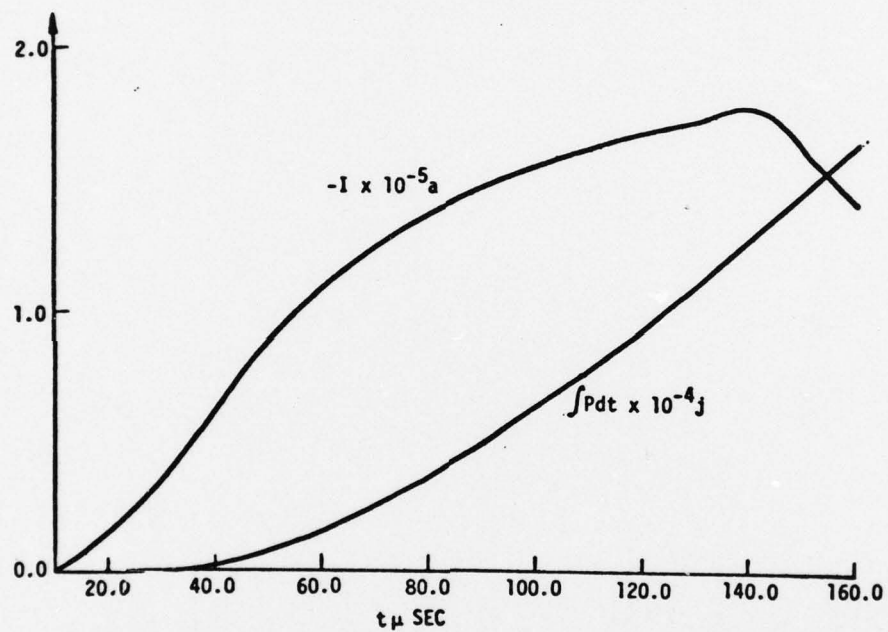
Fig. 2-7b. Evolution of the magnetic field for the case of Fig. 2-7a

8-2865



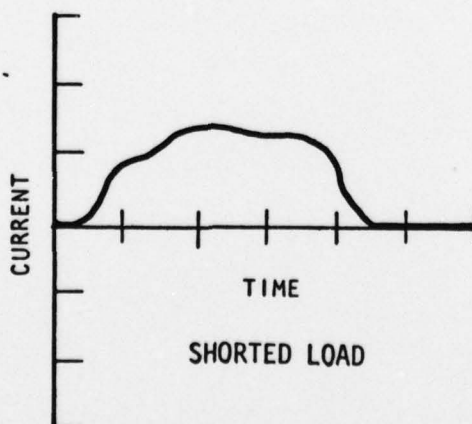
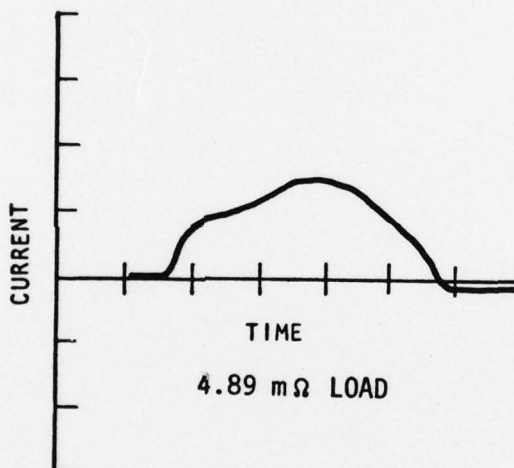
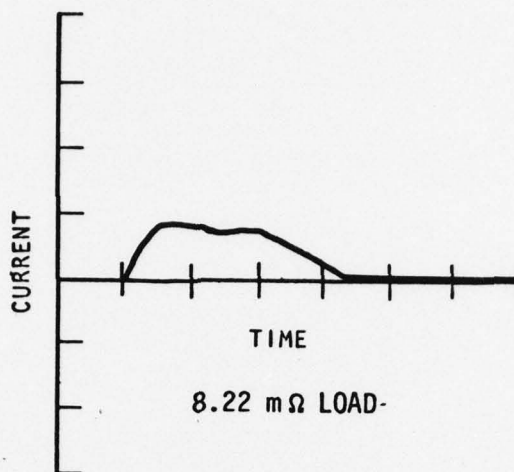
8-2866

Fig. 2-8. Detailed distribution of fluid and electrical variables at $t = 140 \mu s$. Induced magnetic field effects have concentrated the electrothermal instability at the front of the conducting slug.



8-2867

Fig. 2-9. Evolution of the total current and energy during the run shown in Figs. 2-3 and 2-4.



8-2868

Fig. 2-10. Experimentally observed total current pulse shapes from the experiments of Bangerter, et al., [5]. Shift of maximum current to late-time portion of pulse appears to correlate with degree of loading.

3.0 STEADY FLOW: MHD CHANNEL FLOW AT HIGH MAGNETIC REYNOLDS NUMBER

3.1 Flow Structure Prediction in Hydromagnetic Channel Flow

In short burst MHD generator channel flow (timescale $100 \mu\text{s} \sim 1000 \mu\text{s}$) utilizing explosively generated and compressed plasma as a stagnation source [3], the flow is very nearly a steady channel flow. At the plasma conditions of electrical conductivity, length scale, and velocities achievable in such flows both the interaction parameter I (ratio of Lorentz force to change of momentum) and magnetic Reynolds number R_m are large. For the hydromagnetic flows typical of the generators characterized by the operating conditions of Table 3-1 we find the magnetic Reynolds number R_m to be about 20 and the interaction parameter I to be about 15/meter. These conditions indicate that the deceleration time for the fluid is of the order of the diffusion time for the external magnetic field (consisting of applied and possible self-excited combinations) to penetrate through the plasma. One may therefore expect very significant interaction between the velocity field of the flow and the nonuniform Lorentz forces associated with the nonuniform magnetic field diffusion.

In Fig. 3.1 we indicate schematically the interaction of the magnetic field with the high R_m channel flow. The frontal structure (which is not significant over the course of pulses $\geq 10 \mu\text{s}$ and which we will not consider further) consists of axial compression and bending of the magnetic field lines.

Away from the front and throughout the channel, the lines are more sharply bent through the magnetic boundary layers and resemble the cross plane structure shown in Fig. 3.1. At high magnetic Reynolds number the magnetic boundary layers are thin and transverse gradients in y, z are much stronger than axial gradients in x . Correspondingly, the generator current is concentrated in the magnetic boundary layers. At the channel inlet the magnetic field is most strongly excluded from the flow; at the exit the field has penetrated most deeply. We now ask how

TABLE 3-1

Conditions for Illustrative High Magnetic
Reynolds Number Channel Flow

Generator Inlet Conditions

$\langle u \rangle$	$7 \times 10^3 \text{ m/s}$
T	$2.8 \times 10^4 \text{ }^\circ\text{K}$
p	3 k.bar
σ	$5 \times 10^4 \text{ mho/m}$

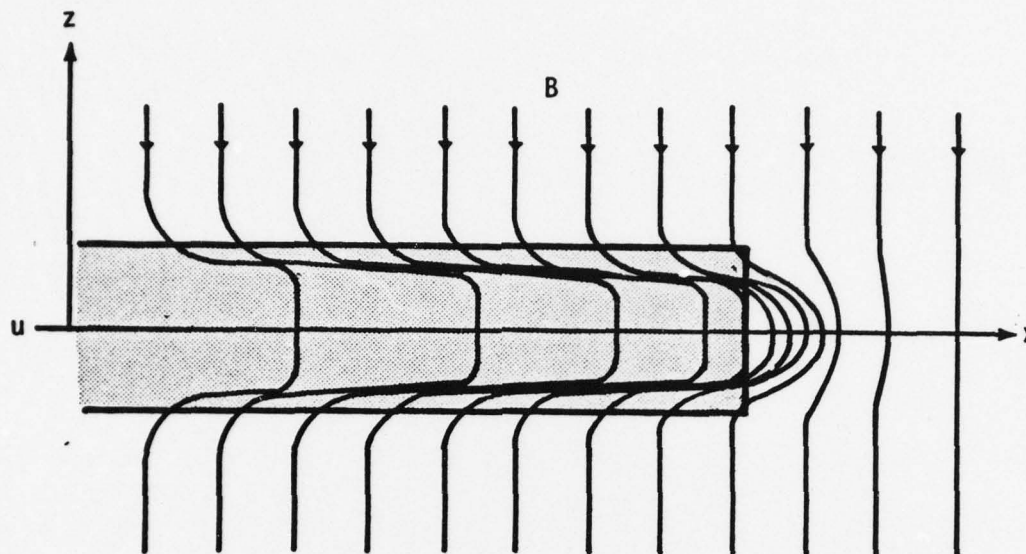
External Magnetic Field (B_0) 10 T

Generator Cross Section (a) 5 cm

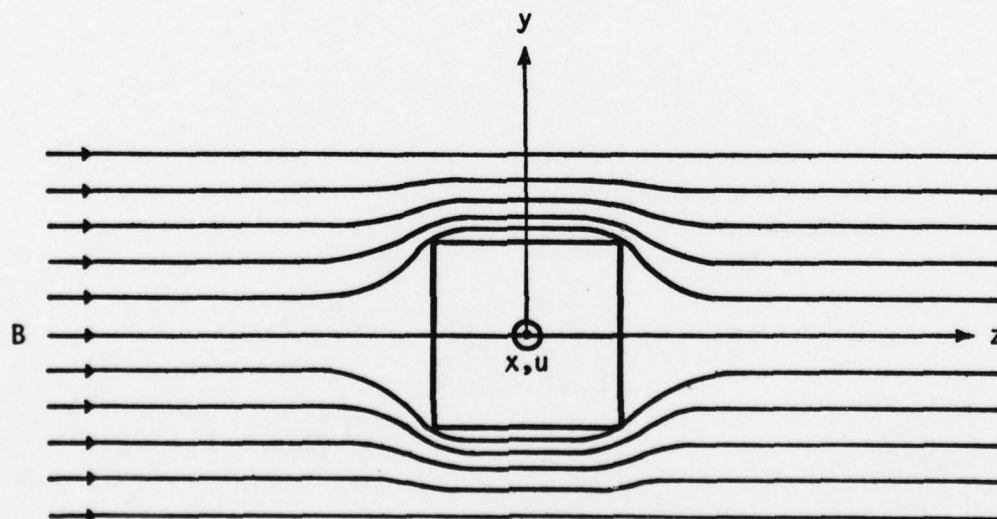
R_m 22

I 15 m^{-1}

8-2869



Axial and Frontal Structure of Magnetic Field
in Hydromagnetic Channel Flow



Cross Plane Structure of Magnetic Field
in Hydromagnetic Channel Flow

8-2870

Fig. 3-1. Magnetic field nonuniformities in high Magnetic
Reynolds Number channel flow

a hydromagnetic flow will respond in its velocity, current, Lorentz force, and power generation distributions to this fundamental nonuniformity situation in high Magnetic Reynolds Number, high interaction parameter flow.

3.2 A Reduced Mathematical Model

We center attention on the axial velocity $u_x(x,y,z)$ and neglect the effects of the cross flow or secondary flow velocity field. Since $I \gg 1$, the flow is dominated by electromagnetic rather than fluid mechanical viscous effects.

Under conditions of $I \gg 1$, $R_m \gg 1$, it is possible to show that the transverse Lorentz force is of order $1/R_m$ times the axial Lorentz force. Hence, cross plane momentum is weakly generated by Lorentz forces compared to axial generation.

The primary source of cross plane velocity nonuniformities is the redistribution of axial mass flow due to the nonuniform deceleration; this is not an insignificant effect, but we expect a quantitative rather than qualitative modification to simulations in which this effect is neglected.

Consistent with our neglect of cross plane momentum, we approximate the axial pressure gradient $\partial p / \partial x$ as $\partial \langle p \rangle / \partial x$ where $\langle \rangle$ indicates an average over the cross section. Mass and momentum conservation lead to

$$\partial_x \langle \rho u \rangle = 0 \quad (3.1)$$

$$u \partial_x u = - \frac{1}{\rho} \partial_x \langle p \rangle + \partial_{\xi_i} (v \partial_{\xi_i} u) + \frac{(\vec{J} \times \vec{B})_x}{\rho} \quad (3.2)$$

where v is the viscous diffusivity, and $\xi_i = (y, z)$ is the cross-plane coordinate. In the case of laminar flow, v is the laminar viscosity; in turbulent flow $v = \alpha q \Lambda$ where q is the RMS turbulence velocity, α is a universal structure parameter, and Λ is the turbulent scale function. In fact, for the conditions of the illustration, viscous effects represent a very small effect for the

momentum balance. The pressure gradient is determined by averaging the momentum equation with $\langle u \partial u / \partial x \rangle \approx 0$:

$$\partial_x \langle p \rangle = \langle (\vec{J} \times \vec{B})_x \rangle - A^{-1} \oint \tau_w ds \quad (3.3)$$

where A is the cross sectional area, τ_w is wall shear stress, and $\oint ds$ represents an integral over the periphery of the cross section.

Let us now consider the electrical description. With $\vec{u} = (u_x, 0, 0)$, Eqs. (2.7) yield

$$u_x \partial_x \vec{B} = -\vec{B} \partial_x u_x + \hat{x} (\vec{B} \cdot \nabla) u_x - \nabla \times (\eta \nabla \times \vec{B}) \quad (3.4)$$

where \hat{x} is the unit vector in the x direction and $\eta = (\mu_0 \sigma)^{-1}$ is the magnetic diffusivity. The boundary conditions for \vec{B} are as follows. As can be seen from Fig. 3-1, specifications of the boundary data for \vec{B} on the channel perimeter requires solution of the external (outside the channel) as well as internal problem for \vec{B} . As an alternative to solution of the external problem, we approximate the boundary conditions for B_y, B_z as

$$\text{on } z = \pm \frac{w}{2} \quad \left\{ \begin{array}{l} B_y = \begin{cases} \mp (B_0 + \Delta B) \exp(-\lambda x) & y > 0 \\ \pm (B_0 + \Delta B) \exp(-\lambda x) & y < 0 \end{cases} \\ B_z = B_0 [1 - \exp(-\lambda x)] \end{array} \right. \quad (3.5)$$

$$\text{on } y = \pm \frac{w}{2} \quad \left\{ \begin{array}{l} B_y = 0 \\ B_z = B_0 + \Delta B \exp(-\lambda x) \end{array} \right. \quad (3.5)$$

where $\lambda = \frac{4\pi^2\eta}{\langle u \rangle} \frac{2}{w^2}$ is the decay term for the fundamental diffusion mode in a square duct, B_0 is the far-field external value of the magnetic field (totally in the z direction), and ΔB is the maximum compression of the magnetic field at the generator inlet. It can be seen that the approximate model (3.5) possesses the correct limiting values at $x \rightarrow \infty$. For $R_m \gg 1$, the values at $x \rightarrow 0$ are also close to the full-field exclusion solutions. The model is least accurate for conditions of $R_m \approx 1$.

For B_x the boundary conditions are $B_x = \pm \mu_0 \frac{I}{2}$ on $z = \pm \frac{w}{2}$ where I is the total current per unit depth flowing in the generator in the transverse direction.

3.3 Magnetic Diffusion and Flow Interaction

We now consider the predictions for flow in the generator channel of Fig. 3-1 under the conditions of Table 3-1. For these conditions we set the generator current at the nominal value

$$I = (1-K) w \langle \sigma u B_z \rangle$$

with $K = 1/2$ and w = the channel width. We assume that no field has penetrated the plasma at the electrode edge $x = 0$. (In general, one will expect a starting magnetic boundary layer thickness at the channel entrance dependent upon the plasma nozzle geometry and the fringe field location.)

The distribution of the transverse current J_y and the magnetic field component B_z for various axial stations in the channel are shown in Fig. 3.2. (There is an axially directed eddy current J_x associated with the fields B_z and B_y which is not shown here.) At $x = 1.4$ cm the magnetic boundary layers are exceedingly thin (≈ 3 mm). They have grown to 1.4 cm at $x = 14$ cm and 2.9 cm at $x = 28$ cm. The inward diffusing magnetic field component B_z is initially concentrated along the walls parallel to the external magnetic field (electrode walls) (see Fig. 3-1b), but the z component on the side walls builds up as the flow proceeds down the channel. The transverse current J_y is initially concentrated along the sidewalls and diffuses inward from these walls.

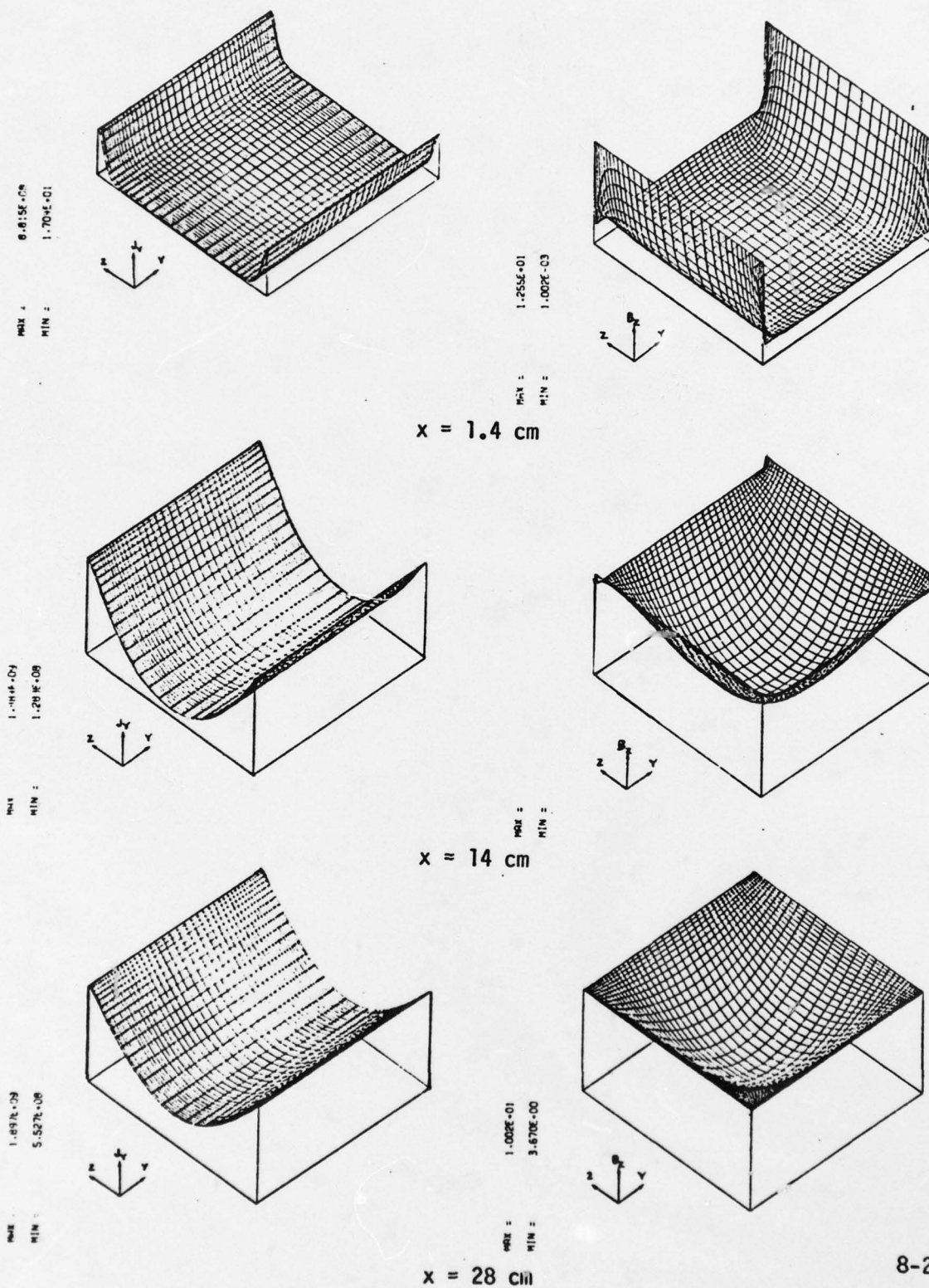


Fig. 3-2. Transverse current and external magnetic field distribution at three axial stations in high Magnetic Reynolds Number channel flow

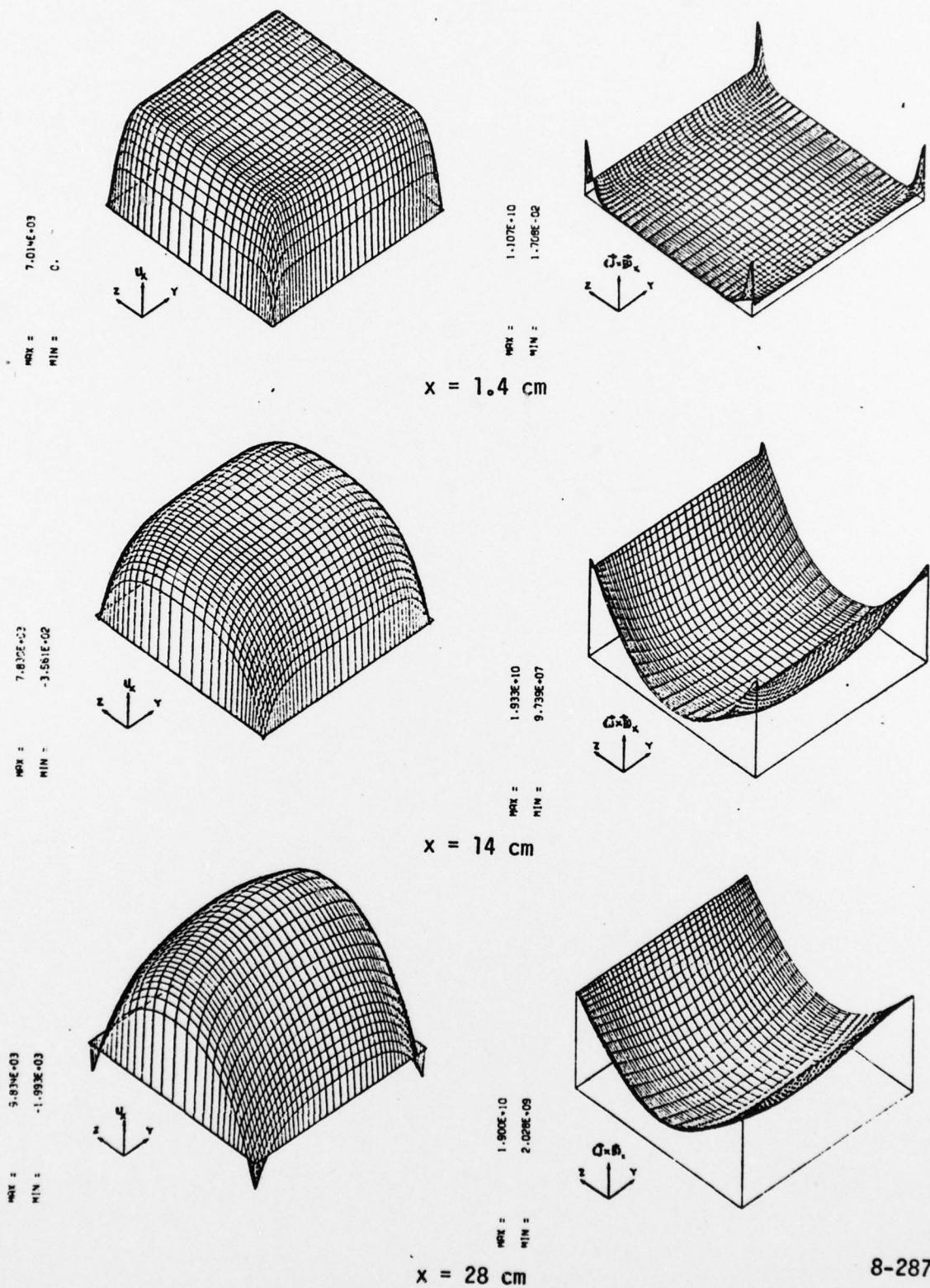
8-2871

In Fig. 3.3 we observe the impact of these distributions of current and magnetic field on Lorentz force and axial velocity. In the early stages of the flow evolution the maximum axial Lorentz force is in the corners. This is because the maximum field B_z exists on the electrode walls parallel to the z axis and maximum current J_y exists on the sidewalls parallel to the y axis. The maximum product of the two therefore exists in the corners. Throughout the entire evolution, the maximum Lorentz force is concentrated in the magnetic boundary layers along the sidewalls.

The impact on the velocity distribution is strong and significant. The initially flat velocity profile is rapidly decelerated in the sidewall layers. By 12 cm the flow is actually reversed in the corners and the regions of reverse flow spread. Because of the deceleration of the wall regions by the inward diffusing Lorentz force the core flow is accelerated. From an initial value of 7 km/s the core flow is accelerated to nearly 10 km/s by $x = 28$ cm. Since there is little Lorentz force in the core region, this high velocity region is not effectively coupled by the generator.

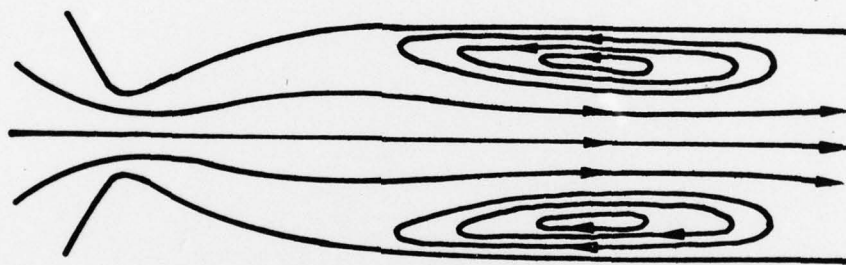
It should be noted that once reverse flow occurs (stalled MHD boundary layers) the present prediction of the actual velocity field in the wall layer region cannot be considered correct since upstream feedback is prohibited by the method of calculation. The present calculation is only definitive in its prediction that stall will indeed occur. In actuality we conjecture that the flow under these conditions will appear as shown in Fig. 3-4 in which recirculation eddies are trapped within the boundary layer region of intense Lorentz force while the core flow jets through outside the region of the eddies. In such a stalled flow, there is little Lorentz force coupling to the high momentum jet in the central region of the channel.

As a demonstration that stall is not a peculiarity of the corner region, we show the Lorentz force and velocity profiles at $x = 21$ cm for a higher interaction situation ($\sigma = 2 \times 10^5$ mho/m) but otherwise conditions identical to Table 3-1 (Fig. 3-5). In Fig. 3-5b we see that the entire sidewall has reversed flow under these conditions.



8-2872

Fig. 3-3. Lorentz force and axial velocity distributions at three axial stations in high Magnetic Reynolds Number channel flow. Wall layers are sharply decelerated with wall layer flows actually reversing. Core flow is accelerated.



9-2895

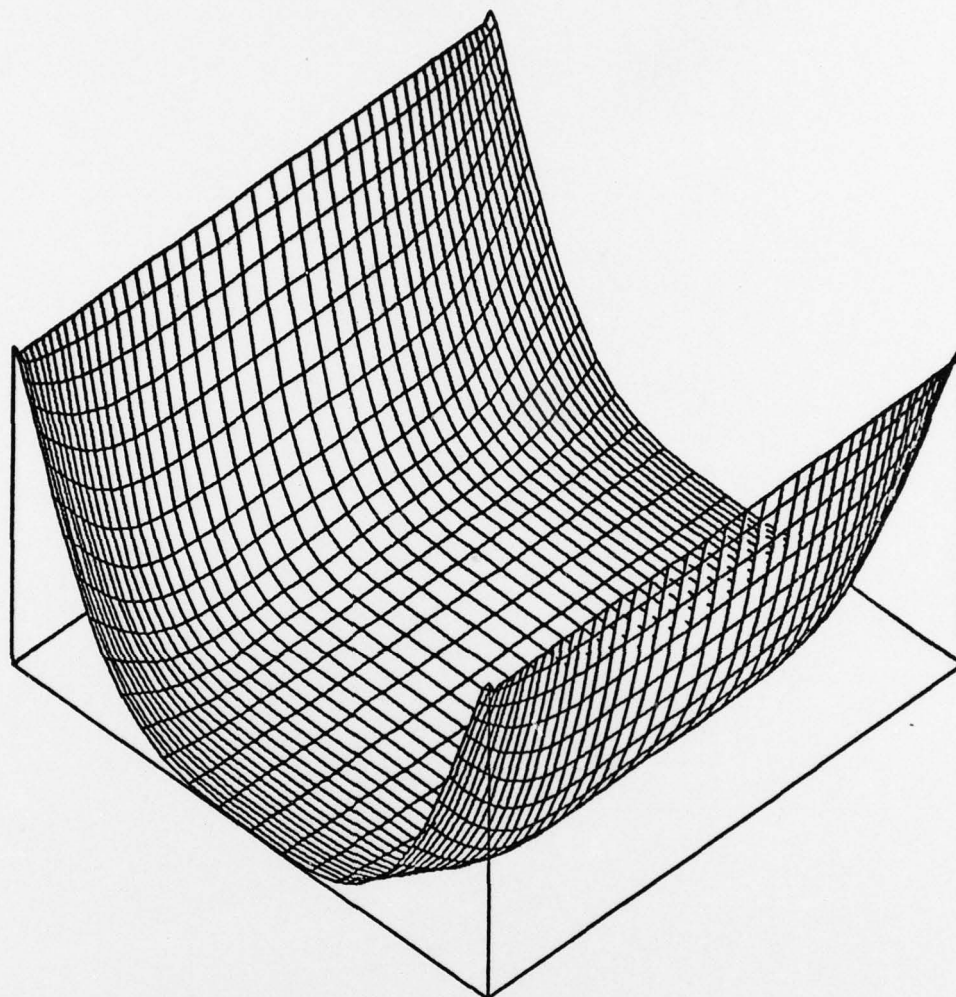
Fig. 3-4. Conjectured velocity streamlines in stalled high Magnetic Reynolds Number channel flow showing recirculation cells trapped in boundary layer region

5.554E+10

4.872E+05

MAX =

MIN =



8-2874

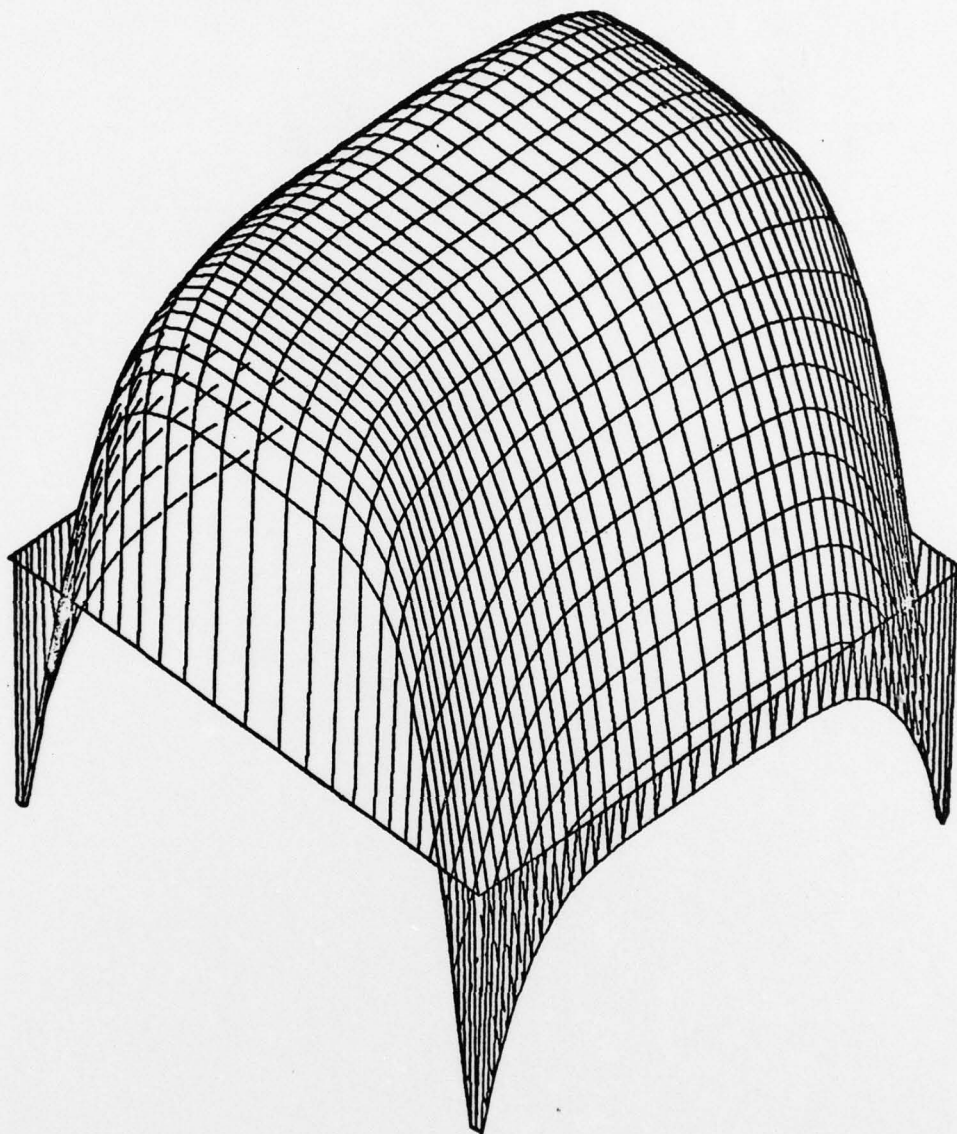
Fig. 3-5a. Lorentz force distribution at $x = 21$ cm corresponding to higher interaction case ($\sigma = 2 \times 10^5$ mho/m) but otherwise conditions as in Table 3-1

9.622E+03

-6.228E+03

MAX =

MIN =



8-2875

Fig. 3-5b. Velocity distribution at $x = 21$ cm corresponding to a higher interaction case ($\sigma = 2 \times 10^5$ mho/m) but otherwise conditions as in Table 3-1. Note that entire sidewall flow is reversed in this case

In Fig. 3-6 we show the distribution of power production $-(\vec{J} \cdot \vec{E})$ over the cross section. Power is only produced in the mid-wall layer regions and is actually consumed in the corner and sidewall layers where reversed flow takes place. The overall power extraction per unit length, dP/dx , is defined as the integral of the power density over the channel cross section:

$$\frac{dP}{dx} = - \int \int_A (\vec{J} \cdot \vec{E}) d^2x$$

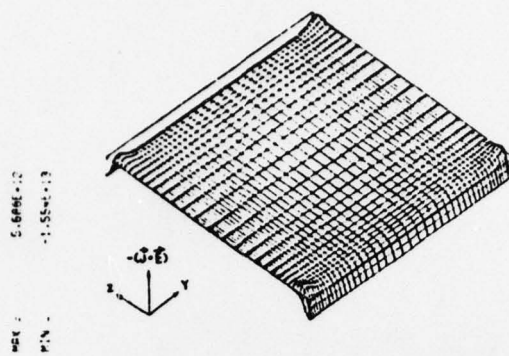
The ideal power extraction for uniform flow is

$$\left(\frac{dP}{dx} \right)_{\text{ideal}} = K(1-K) \sigma u_0^2 B_0^2 A$$

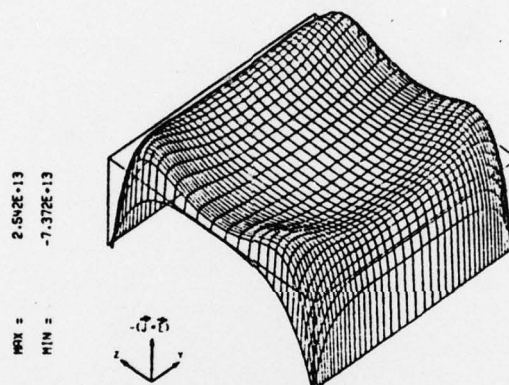
In Fig. 3-7 we exhibit the ratio of these quantities for the conditions of Table 3-1. It can be seen that for a channel 15 cm long, only 10% of the ideal power is available and for a 28 cm channel only 27% is available. These results must be tempered by the observation that beyond 12 cm the boundary layers have begun to stall; it is not likely that power extraction will be enhanced by realistic inclusion of the recirculation zones under stalled conditions. Hence, the power extraction levels beyond $x = 12$ cm will likely not be reached.

It is appropriate to mention at this stage that previous experiments at Hercules, Inc. on pulsed MHD generators failed to correlate with the conductivity computed by Hercules, Inc., and their consultants. The conductivity computed by Hercules, Inc. was too high.

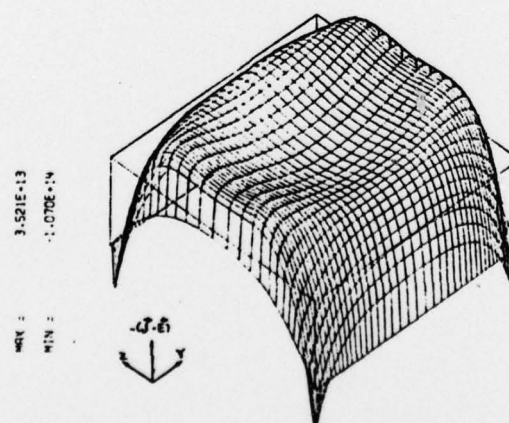
However, when the STD Research theory and conductivity calculations were used with the same inputs, the calculated conductivity was approximately 40% lower and there was excellent agreement with experiments.



$x = 1.4 \text{ cm}$



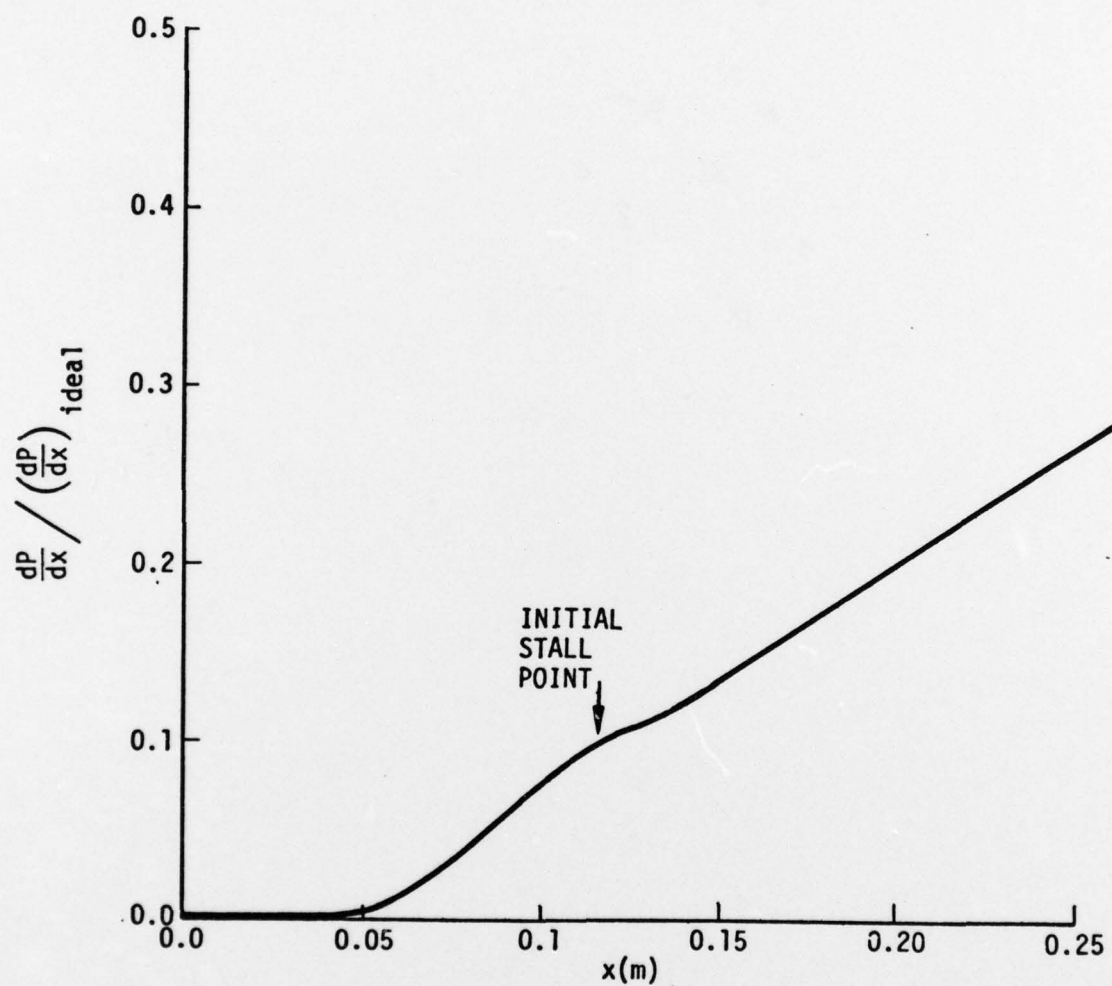
$x = 14 \text{ cm}$



$x = 28 \text{ cm}$

8-2876

Fig. 3-6. Power extraction density evolution for the case in Figs. 3-2 and 3-3. Power is produced in m layer and core regions but consumed in near wall regions



8-2877

Fig. 3-7. Ratio of power extraction per unit length to ideal power extraction. Wall layers stalled over most of channel length

REFERENCES

- [1] Jones, M., "Explosion Driven Linear MHD Generators," Proc., of The Conference on Megagauss Magnetic Field Generation by Explosives, Frescati, Italy, Sept. 1965
- [2] Bangerter, C. D., B. D. Hopkins, and T. R. Brogan, "Explosively Driven Power Generation: A Progress Report," 6th Int'l. Conf. on Magnetohydrodynamic Electrical Power Generation, Washington, D.C., Vol. IV, No. CONF-750601-P4, p. 155, June 1975
- [3] Gill, S. P., D. W. Baum, and H. Calvin, "Explosive MHD Research" Artec Assoc., Annual Rpt. No. 119AR to ONR, April 1975 - 1 April 1976
- [4a] Demetriades, S. T., G. S. Argyropoulos, and C. D. Maxwell, "Progress in Analytical Modeling of MHD Power Generation," Proc., 12th Symposium on Engineering Aspects of Magneto-hydrodynamics, Argonne Nat'l. Lab., Argonne, IL, pp. I.5.1 - I.5.13, March 1972
- [4b] Argyropoulos, G. S., M. A. Casteel, and S. T. Demetriades, "Two-Dimensional Distribution of Current Along Magneto-hydrodynamic Channels," Energy Conversion, Vol. 10, pp. 189-192, Pergamon Press, 1970
- [5] Markham, D. M., C. D. Maxwell, S. T. Demetriades, and D. A. Oliver, "A Numerical Solution to the Unsteady, Quasi-Three-Dimensional, Turbulent Heat Transfer Problem in an MHD Channel," AICHE-ASME Heat Transfer Conf., Paper No. 77-HT-90, Salt Lake City, UT, April 1977
- [6] Oliver, D. A., and C. D. Maxwell, "Interaction of Magnetohydrodynamic Plasma with Boundaries," AIAA 15th Aerospace Sciences Mtg., Paper No. 77-108, Los Angeles, CA, January 1977
- [7] Maxwell, C. D., D. M. Markham, S. T. Demetriades, and D. A. Oliver, "Coupled Electrical and Fluid Calculations in the Cross Plane in Linear MHD Generators," Proc., 16th Symposium on Engineering Aspects of Magnetohydrodynamics, Univ. Pittsburgh, pp. VII.3.13 - VII.3.20, May 1977
- [8] Gill, S. P., D. W. Baum, W. Schimmin, and D. Mukherjee, "Explosive MHD Research," Artec Assoc., Final Report No. 119, to ONR, 1 April 1976 - 1 April 1977

References, (cont'd)

- [9] "Pulsed Magnetohydrodynamic Program," Hercules, Inc., Systems Group, Bacchus Works, Final Rpt. No. AFAPL-TR-76-34 for Period 3, to Air Force Aero Propulsion Lab., January 1972 to March 1976, dated July 1976
- [10] Nelson, H. F., "Nonequilibrium Structure of Argon Shock Waves," Phys. Fluids, Vol. 16, No. 12, p. 2132, December 1971
- [11] Foley, Wm. H., and J. H. Clarke, "Shock Waves Structures by Nonequilibrium Ionizing and Thermal Phenomena," Phys. Fluids, Vol. 16, No. 3, pp. 375-383, March 1973
- [12] Maksimov, A. A. and V. E. Ostashev, "Breakdown of the Gas Ahead of a Shock Front in an Induced Electric Field," High-Temperature Institute, Academy of Sciences of the U.S.S.R., Trans. from Teplofizika Vysokikh Temperatur, Vol. 13, No. 3, pp. 644-647, May-June, 1975
- [13] Demetriades, S. T., and G. S. Argyropoulos, "Ohm's Law in Multi-component Nonisothermal Plasmas with Temperature and Pressure Gradients," Phys. Fluids, Vol. 9, No. 11, pp. 2136-2149, November 1966
- [14] Demetriades, S. T., C. D. Maxwell, G. S. Argyropoulos, and G. Fonda-Bonardi, "Influence of Controlled Turbulence on Gaseous Discharges," Proc., 11th Symposium on Engineering Aspects of Magnetohydrodynamics, Caltech, Pasadena, CA, March 1970
- [15] Oliver, D. A., "A Constricted Discharge in Magnetohydrodynamic Plasma," Proc., 15th Symposium on Engineering Aspects of Magnetohydrodynamics, Univ. Pennsylvania, Philadelphia, p. IX.4, May 1976
- [16] Levine, M. A., "Turbulent Mixing at the Contact Surface in a Driven Shock Wave," Phys. Fluids, Vol. 13, No. 5, pp. 1166-1171, May 1970
- [17] Glass, I. I., S. K. Chan, and H. L. Brode, "Strong Planar Shock Waves Generated by Explosively-Driven Spherical Implosions," AIAA J., Vol. 12, No. 3, pp. 367-374, March 1974

ONR PULSED POWER PROGRAM

DISTRIBUTION LIST

Defense Documentation Center (12)
Building 5
Cameron Station
Alexandria, VA 22314

Dr. E. T. Florance
Office of Naval Research Branch Office
1030 East Green Street
Pasadena, CA 91106

Mr. J. A. Satkowski (3)
Office of Naval Research
Code 473
Arlington, VA 22217

Mr. John Siambis
Office of Naval Research
Code 421
Arlington, VA 22217

Naval Research Laboratory (6)
Code 2627
Washington, DC 20375

Naval Research Laboratory (6)
Code 2629
Washington, DC 20375

Dr. P. Turchi
Naval Research Laboratory
Code 6770
Washington, DC 20375

Dr. A. E. Robson
Naval Research Laboratory
Code 6708
Washington, DC 20375

Mr. Franklin R. Smith
Army Corps of Engineers
Code HNDED-SR
P.O. Box 1600
Huntsville, AL 35807

Mr. Robert Dannenburg
NASA Ames Research Center
Code NS229-4
Moffett Field, CA 94035

Dr. David Fenneman
Naval Surface Weapons Center
Code FI2
Dahlgren, VA 22448

Dr. T. L. Berger
Naval Surface Weapons Center
Code FI2
Dahlgren, VA 2448

Dr. George Ullrich
Headquarters
Defense Nuclear Agency
Washington, DC 20305

Mr. John Farber
Headquarters
Defense Nuclear Agency
Washington, DC 20305

Dr. Terry Godlove
Department of Energy
Code C-404
Washington, DC 20545

Dr. Joseph Mangano
Defense Advanced Research
Projects Agency
Strategic Technology Office
1400 Wilson Boulevard
Arlington, VA 22209

Dr. F. J. Rogers
Lawrence Livermore Laboratory
H - Division
P. O. Box 808
Livermore, CA 94550

Dr. Marvin Ross
Lawrence Livermore Laboratory
H - Division
P. O. Box 808
Livermore, CA 94550

Dr. Richard More
Lawrence Livermore Laboratory
H - Division
P. O. Box 808
Livermore, CA 94550

Dr. Harold Graboske
Lawrence Livermore Laboratory
L 355
P.O. Box 808
Livermore, CA 94550

Dr. Hugh E. DeWitt
Lawrence Livermore Laboratory
P. O. Box 808
Livermore, CA 94550

Dr. William Nellis
Lawrence Livermore Laboratory
L 355
P.O. Box 808
Livermore, CA 94550

Mr. William Cowan
Sandia Laboratories
P.O. Box 4230
Albuquerque, NM 87510

Dr. R. F. Flagg
Physics International
2700 Merced Street
San Leandro, CA 94577

Professor S. Winterberg
University of Nevada
Desert Research Institute
Reno, NV 89507

Dr. M. Kristiansen
Texas Tech University
Department of Electrical Engineering
Lubbock, TX 79409

Dr. Peter Ottenger
Thermo Electron Corporation
101 First Avenue
Waltham, MA 02154

Mr. C. D. Bangerter
STD Corporation
P.O. Box C
Arcadia, CA 91006

Dr. David Oliver
STD Corporation
P.O. Box C
Arcadia, CA 91006

Mr. Thomas F. Swean, Jr.
STD Corporation
P.O. Box C
Arcadia, CA 91006

Dr. Dennis W. Baum
Artec Associates, Inc.
26046 Eden Landing Road
Hayward, CA 94545

Dr. Deb Mukherjee
Artec Associates, Inc.
26046 Eden landing Road
Hayward, CA 94545

Dr. Stephen P. Gill
Artec Associates, Inc.
26046 Eden Landing Road
Hayward, CA 94545

Prof. Horst Wilhelm
University of Florida
Department of Engineering Sciences
Gainesville, FL 32601

Dr. B. Zauderer
General Electric Company
Valley Forge Space Center
P.O. Box 8555
Philadelphia, PA 19101

Dr. E. Tate
General Electric Company
Valley Forge Space Center
P.O. Box 8555
Philadelphia, PA 19101

Dr. Jay P. Boris
Naval Research Laboratory
Laboratory for Computational Physics
Code 6020
Washington, DC 20375